MICROSTRUCTURE AND PARTICLE ARRANGEMENT IN THREE DIMENSIONAL PRINTING

by

ALAN J. LAUDER

B.S. Engineering Science, The Pennsylvania State University
(1990)

Submitted to the Department of
Materials Science and Engineering in
Partial Fulfillment of the Requirements
for the Degree of

MASTER OF SCIENCE

in Materials Engineering
at the

Massachusetts Institute of Technology

September 1992

Signature of Author _____
Department of Materials Science and Engineering
August 7,1992

Certified by _____
Michael J. Cima
Norton Associate Professor of Ceramics
Thesis Supervisor

Accepted by _____
Linn W. Hobbs
Professor of Materials Science
Chairman, Departmental Committee on Graduate Students

MICROSTRUCTURE AND PARTICLE ARRANGEMENT IN THREE DIMENSIONAL PRINTING

by

ALAN J. LAUDER

Submitted to the Department of Materials Science and Engineering
on August 7, 1992 in partial fulfillment of the requirements
for the Degree of Master of Science
in Materials Engineering

ABSTRACT

Three Dimensional Printing is a solid freeform fabrication process being developed for the direct manufacture of functional tooling and prototypes from a computer solid model. The process functions by selectively binding areas of a thin layer of powdered material and sequentially building layers until the desired three dimensional shape is achieved. The binder material is deposited by a printhead using a variation on ink-jet printing technology which is scanned over the powder layer in a raster pattern. After all layers have been formed, the unbound powder is removed leaving the three dimensional part. The microstructure of the finished part is determined by several factors such as binder and powder material, post-forming heat treatment, and powder/binder interactions.

An extensive microstructural analysis was performed on parts made using alumina powders and a colloidal silica binder. These materials can be used to produce glass refractory parts suitable for use as shells and cores for metals casting. Microstructural processes that occur during printing were identified by investigating the morphology and properties of primitive elements resulting from simple powder/binder interactions, such as the result of a single droplet of binder being deposited in the powder bed. Increasingly more complex elements were analyzed to achieve an understanding of the entire process. Analytical techniques included optical and electron microscopy for morphology, mercury porosimetry for pore size and particle packing, and helium pychnometry for density and composition. The effect of the chemical additives to the powder bed was also studied.

Results of microstructural analysis show that many factors affect the microstructure of a Three Dimensional Printed part, including surface tension forces, raster scan dimensions, layer thickness and effective pH of the powder bed. Evidence is also found that many aspects of the microstructure may be controllable through chemical or physical processes, some of which may be coded into the governing computer file.

Thesis Supervisor: Dr. Michael J. Cima

Title: Norton Associate Professor of Ceramics

ACKNOWLEDGMENTS

I would like to thank Professor Michael Cima for his expert guidance and support over the past year and a half, and for his patience and tutelage as I entered this new field of ceramics.

I would also like to thank Professor Emmanuel Sachs of the Department of Mechanical Engineering for his advice and suggestions for experiments, which were invaluable in maintaining the focus of this work.

Every member of the Three Dimensional Printing team contributed in some way to this thesis and made my time here more enjoyable. In particular, special thanks are due to Dave Brancazio for his help in running the machine and with the building of the primitive generating circuit.

Tailin Fan, my two-time co-author, deserves a large amount of credit for conceiving of and sparking interest in the study of single droplet powder-binder interactions. Good luck with your continued work in the field.

Jim Bredt, thanks for all your help with trouble shooting and your suggestions on technical matters.

Satbir Khanuja and Steve Michaels, thanks for all the conversations and ideas on the materials issues, as well as those on less relevant topics.

Thanks are also due to John Lee, who allowed me to borrow his data and conclusions to help me make some of my own points.

Alain Curodeau, Klaus Kremmin, Jill Milner, Harald Tuerck and everybody else in the 3DP group all deserve thanks for helping out and making my work easier.

My officemates, Dr. Simone Peterson and Bryan Blackwell, have my gratitude and friendship for making MIT a much more fun place to be.

John Centorino and Lenny Rigione, thanks for helping me learn how to use all the equipment in Building 12.

I appreciate the help from everybody at CPRL and MPC. Dr. Dick Pober and Dr. Zhiping Jiang deserve special thanks for all their advice and assistance.

To my parents, thank you for providing all the love and support I needed throughout my education, and for taking such a strong interest in my accomplishments. And to my future wife Heather, thanks for all the love, understanding, and patience you've given me every day for almost three years.

Financial support for this work was provided by the Strategic Manufacturing Initiative of the National Science Foundation, and by the Three Dimensional Printing Consortium.

CONTENTS

LIST OF FIGURES

LIST OF TABLES

1. INTRODUCTION

1.1 Rapid Prototyping

The increasingly competitive global market forces manufacturers to move quickly if they want to stay in business. Reducing product development time from conception to first sales (time to market) has become essential for maintaining a competitive edge for technological and consumer product industries. Being first in the marketplace has several advantages, including greater profits due to higher initial prices and increased market share, an innovative image, and attraction of quality people (Staelin, 1992). An early entry into the market also increases the effective product life before obsolescence; an important factor with today's shortening product lifetime cycles due to rapid technological advances and stylistic changes (Qualls, 1981).

Prototyping is an essential step in product development. A successful prototyping strategy will reduce the cost, risk, and time necessary to bring a new product to the market (Eagar, 1992). It has been found that prototyping is the development activity most closely linked with product success (Hise, 1989). The advent of desk top manufacturing and rapid prototyping technology which produce parts directly from a computer model can provide businesses with an extremely powerful tool to streamline their development efforts. Rapid prototyping now offers a wide range of possible systems using different materials and techniques. Commercial rapid prototyping systems currently produce parts made of plastic or paper. Future systems now under development will utilize metal and ceramics as building materials. Research into the materials capabilities of these new technologies is becoming increasingly important because the effectiveness of a prototyping effort depends on the selection of a fabrication method and a functional material (Hom, 1991).

1.2 Materials Science in Rapid Prototyping

The functionality of a prototype depends on the material from which it is made and the process used to make it. For example, a plastic part may be adequate for look-and-feel type evaluation, but cannot be used to test high temperature performance. Materials research in the area of rapid prototyping will identify new materials for rapid prototyping and will improve the properties of currently available systems. Fundamental process understanding based on materials science and microstructural analysis is necessary to fully realize the full potential of these technologies. This knowledge will allow better process design for improved microstructural features such as finer surface finish, elimination of strength limiting flaws, and compositional control.

These new techniques may also be used to produce parts impossible to make by traditional manufacturing methods. For example, Three Dimensional Printing may be used to produce very fine enclosed channels or designed pore networks in ceramic and metal parts that cannot be obtained by traditional processing methods. Integration of these fine features into a part requires an understanding of the basic microstructural processes which occur during printing. Fine process control coupled with knowledge of rudimentary microstructural development may allow designers to specify macroscopic characteristics (such as geometry, dimensions, and tolerances) as well as microstructural features (such as composition, porosity, and grain size) simultaneously. The use of computer aided design (CAD) and computer process control may allow storage of the specifications in a data file which in turn may be used to build a part with the desired features without intervention by an engineer. These ideas have already been realized for macroscopic features but further research in materials science and engineering is necessary before computer derived microstructures will be possible.

1.3 Purpose

This thesis presents an analysis of the microstructural processes and resulting structures that are important in Three Dimensional Printing of ceramic parts. 3D Printed

parts are produced by a serial process in which small units of powdered material are sequentially joined by a liquid binder. The joining of small units continues until a part with the desired geometry and dimensions is completed. The properties of the individual units of bound powder play a large role in determining the microstructure of the entire part. The analysis presented here seeks to determine how these individual units are created, and how they join to each other to create a macroscopic structure. The development of the microstructure is investigated from the simplest units of joined powder to complete parts. Furthermore, the mechanisms which control microstructural formation are determined and process parameters which affect these mechanisms are examined.

2. BACKGROUND

2.1 Solid Freeform Fabrication

Solid Freeform Fabrication (SFF) has been defined as "the production of freeform solid objects directly from a computer model without part-specific tooling or human intervention" (Bourell, Beaman, Marcus, and Barlow, 1990). Solid Freeform Fabrication methods are ideal for manufacturing small numbers of unique components, or for rapid prototyping because they eliminate the need for tool production. Several technologies to produce parts by SFF have been developed in recent years, using widely different methods and materials. A common aspect of these systems is that parts are constructed by a laminated building process. A solid model computer file is sliced to produce two dimensional cross sections of the object to be made. The object is then built layer by layer using these two dimensional slices to guide the fabrication process. Solid Freeform Fabrication techniques produce unique microstructures, just as traditional machining or casting processes. This thesis focuses on microstructure in Three Dimensional Printing, but an overview of the Solid Freeform Fabrication field is presented below.

2.2 Related Work

Stereolithography

Stereolithography builds solid plastic parts by using a UV laser to selectively polymerize acrylate liquid photopolymers. The Laser Stereolithography Apparatus (SLA) made by 3D Systems (Valencia, CA) was the first SFF system to become commercially available. SLA scans a UV laser across a bath of photopolymerizable polymer using galvanometer controlled mirrors to move the laser beam. The scanned polymer becomes partially cured, and is supported from underneath by a flat surface attached to an elevator. The elevator then lowers, permitting fresh polymer flow over the part in progress creating a level for a new layer. The SLA system is illustrated in Figure 2.1.

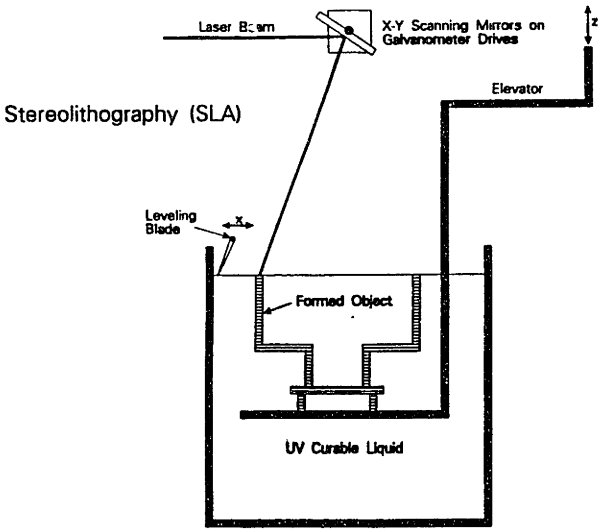

Figure 2.1 Stereolithography Apparatus with part being built.

As with any fabrication method, the processing steps in Stereolithography have an effect on the microstructure of the product. Three examples can be seen in parts built by SLA. A basic example of processing influence on the microstructure is caused by the use of a laser to cure the polymer. Since the laser beam varies in intensity over its cross section, the polymer in the center of the beam cures more quickly and to a greater depth than the polymer at the edges. This effect gives the scanned lines a v-shaped cross section known as a "bullet." Figure 2.3 shows this effect as predicted by a mathematical model developed at the University of Dayton (Flach and Chartoff, 1990). Figure 2.4 is an optical micrograph of the polished edge of an SLA part, showing a bullet at the edge of each layer. The most noticeable example of a processing/microstructure connection is the layering of the part, a feature common to many SFF processes. In addition, SLA parts have rounded corners, not perfectly sharp ones. This feature is due to the movement of the mirrors by the galvanometer which must occur at a finite speed. Figure 2.2 is a micrograph of an SLA part displaying these two features.

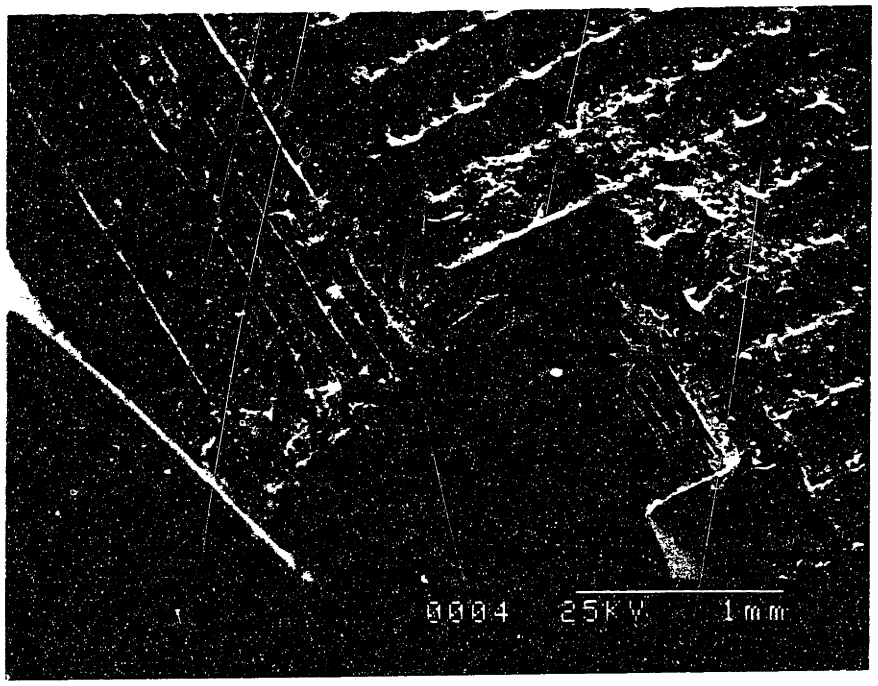

Figure 2.2 Micrograph of the corner of an SLA part showing layers and rounded corners.

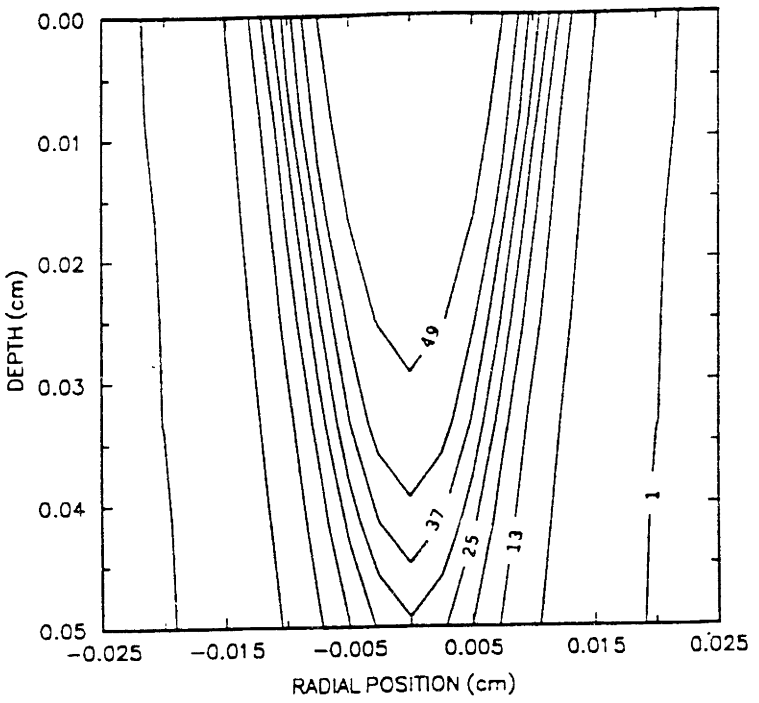

Figure 2.3 Contour plot showing % conversion of monomer as a function of position, from a mathematical model for laser photopolymerization. Time of exposure = 0.3 sec; Contour interval = 6%. (Flach and Chartoff, 1990)

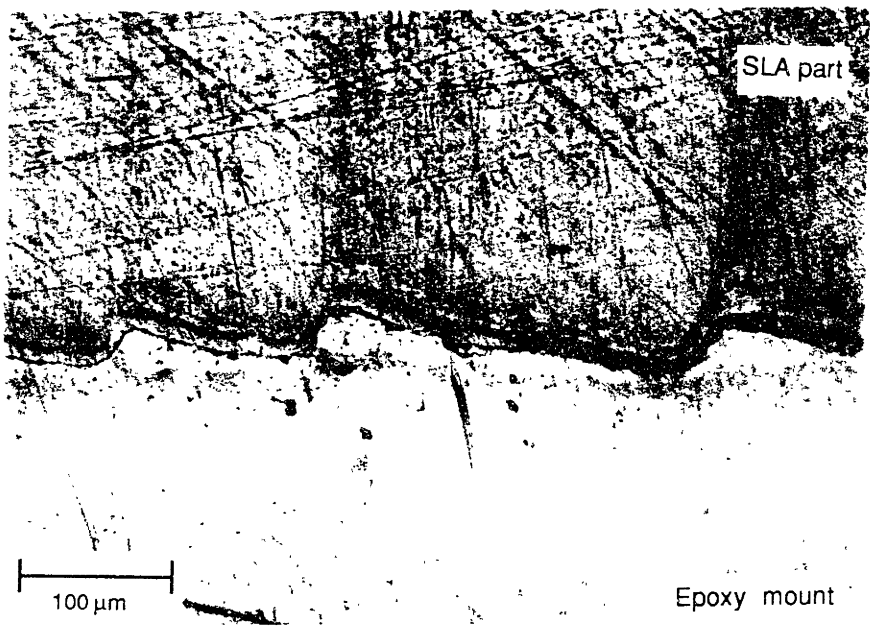

Figure 2.4 Optical micrograph of the edge of an SLA part that has been mounted and polished to reveal surface topography. Bullets are visible at the edge of each layer.

Selective Laser Sintering

Selective Laser Sintering (SLS) builds parts by scanning a 25 watt CO_2 laser across a layer of powder supported by a base. The beam intensity is varied to cause the powder to melt or sinter together in selected areas. After scanning, the base is lowered and a new layer of powder is deposited. The process repeats layer by layer until the part is finished. Selective Laser Sintering is commercially available for use with poly-carbonate, PVC, and wax powders from DTM Corporation (Austin, TX). Use of metal and ceramic powders with SLS is under development (Lakshminarayan, Ogrydiziak, and Marcus, 1990; Manriquez-Frayre, Bourell, 1990).

Some of the microstructural processes that are important in SLS are similar to those in Stereolithography. Both systems use galvanometer-controlled mirrors to drive a laser beam, resulting in related groups of features. SLS is also affected by several materials features, including particle size, thermal diffusivity, melting temperature, and energy beam coupling (Marcus, Beaman, Barlow, and Bourell, 1990). Another process

important in Selective Laser Sintering is localized heating and cooling at high rates, which can lead to residual stresses. In order to reduce residual stress, the powder bed must be heated during building to the annealing temperature of the material. These elements of the SLS process all show an effect on the final part microstructure.

Fused Deposition Modeling

Fused Deposition Modeling extrudes polymer filaments through an x-y head to build solid objects (Ashley, 1990). Manufactured by Stratasys Inc. (Minneapolis, MN), the fused deposition 3D Modeler feeds a filament of thermoplastic material such as nylon or wax through a heated extruder head. The head melts the polymer and extrudes it onto an elevator following an x-y pattern similar to a number-controlled tool path. Layers are generated by lowering the elevator and repeating the process. Fused Deposition Modeling has the advantage that it requires no lasers, toxic materials, or post-process heat treatment, but it is limited to low T_g extrudable thermoplastics and residual stresses due to cooling must be accounted for.

Laminated Object Manufacturing

Laminated Object Manufacturing (LOM) uses a CAD-model guided laser to cut 2D cross sections out of a rolled sheet material (Rapid Prototyping Report, 1991). The LOM machine, made by Helisys, Inc. (Torrance, CA), can be used to make parts out of paper, plastic, metal sheet stock, or ceramic tape. The process works by placing a sheet of material from a continuous roll over the work area. The laser cuts out the 2D cross section for a single layer and then cuts the remaining sheet into small squares, called tiles, for later removal. A fresh section of sheet is fed into the work area, and the process repeats. Layers are bonded together by passing a hot roller over a completed layer to activate a previously applied adhesive coating, forming a laminated three dimensional part. Figure 2.5 is a schematic diagram of the LOM machine.

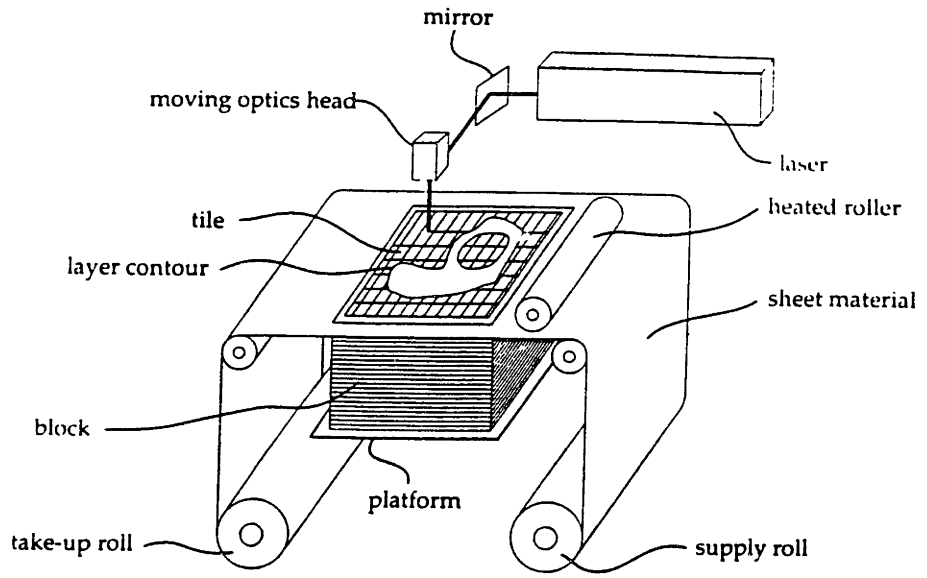

Figure 2.5 Configuration of a Laminated Object Manufacturing machine. (Rapid Prototyping Report, 1991)

The laminated structure of LOM parts, which consists of alternating layers of adhesive and paper or metal, gives rise to large anisotropies in material properties. Strength and modulus can vary depending on the direction of the applied stress. Delamination failures must also be considered when subjecting LOM components to loading. Therefore, the microstructure of the part, particularly at the interfaces, has a large effect on how such a component may be used.

Other Technologies

Several other Rapid Prototyping technologies are under development. Diverse strategies such as photolithography of layers, discrete particle beams, and vapor phase deposition are being used. Cubital America's (Warren, MI) Solider system uses a previously prepared set of masks to expose and cure a photosenstitive polymer. Three dimensional parts are built by stacking layers of the cured polymer. Ballistic Particle Manufacturing, under development by Perception Systems (Easley, SC), injects droplets

of a thermoplastic material onto a movable x-y table where they solidify to form a three dimensional part. Selective Area Laser Deposition (Jacquot, Zong, and Marcus, 1990) uses a laser in a CVD reactor to locally heat a substrate and grow the product in selected areas. All of these techniques are being developed to produce three dimensional parts without part-specific tooling or human intervention. Table 2.1 presents a summary of the related technologies.

Table 2.1 Summary of Related Technologies

Name	Maker	Materials	Process
Stereolithography	3D Systems Valencia, CA	photosensitive acrylate polymers	UV Laser scan to selectively polymerize liquid resins
Selective Laser Sintering	DTM Corp. Austin, TX	thermoplastic polymer powders, metal and ceramic powders	CO_2 laser to selectively melt or sinter powdered materials
Fused Deposition Modeling	Stratasys Inc. Minneapolis, MN	thermoplastic nylon and wax filaments	Hot extrusion of thermoplastic filaments following an NC tool path
Laminated Object Manufacturing	Helisys Inc. Torrance, CA	paper, plastic, and metal sheet stock	Laser cutting of 2D cross sections out of sheet materials which are stacked for a 3D part
Solider	Cubital America Warren, MI	photosensitive polymers	Variation on photolithography to produce layers of cured photopolymer
Ballistic Particle Manufacturing	Perception Systems Easley, SC	organic waxes	Injection of discrete droplets onto a movable x-y table.
Selective Area Laser Deposition	University of Texas Austin, TX	acetylene precursor for CVD of carbon	Laser enhanced CVD locally heats substrate to form reaction products selectively

2.3 Three Dimensional Printing

Process Description

Three Dimensional Printing is a manufacturing process for the rapid production of three dimensional parts directly from computer models (Sachs, Cima, Williams, and Brancazio, 1990). This process creates a solid object by printing sequential two-dimensional layers. Each layer begins with distribution of powder over the surface of a powder bed. A slicing algorithm obtains detailed information for every layer from a computer model of the desired part. Selective application of a liquid binder joins particles where the object is to be formed using a technology similar to ink-jet printing. Printing is accomplished by moving a printhead over the powder bed in a raster-scan pattern. The binder jet is composed of droplets which are allowed to fall onto the powder bed in areas where the powder is to be joined. In areas that are not to be joined, the droplets are charged and electrostatically deflected onto a catcher which prevents them from hitting the powder. A piston which supports the powder bed and the part in progress then lowers so that the next powder layer can be spread and selectively joined. This layer-by-layer process repeats until the part is completed. Following a heat treatment, the unbound powder is removed, leaving the fabricated part. The sequence of operations is depicted in Figure 2.6.

Binder is delivered to the powder through a continuous-jet type ink-jet printhead. A continuous stream of liquid binder passes through a nozzle with a 0.34 mm orifice. A piezoelectric disk attached to the nozzle is caused to vibrate at 50 to 60 kHz, inducing instabilities in the jet which cause it to break up into small droplets about 75 μm in diameter at a frequency synchronized with that of the piezo. The droplets pass through the center of a cylindrical capacitor as they are formed, where they can be selectively charged by computer control of the capacitor voltage. The droplets then pass between a high voltage plate and a ground plate. The electric field in this region deflects charged droplets horizontally, while uncharged

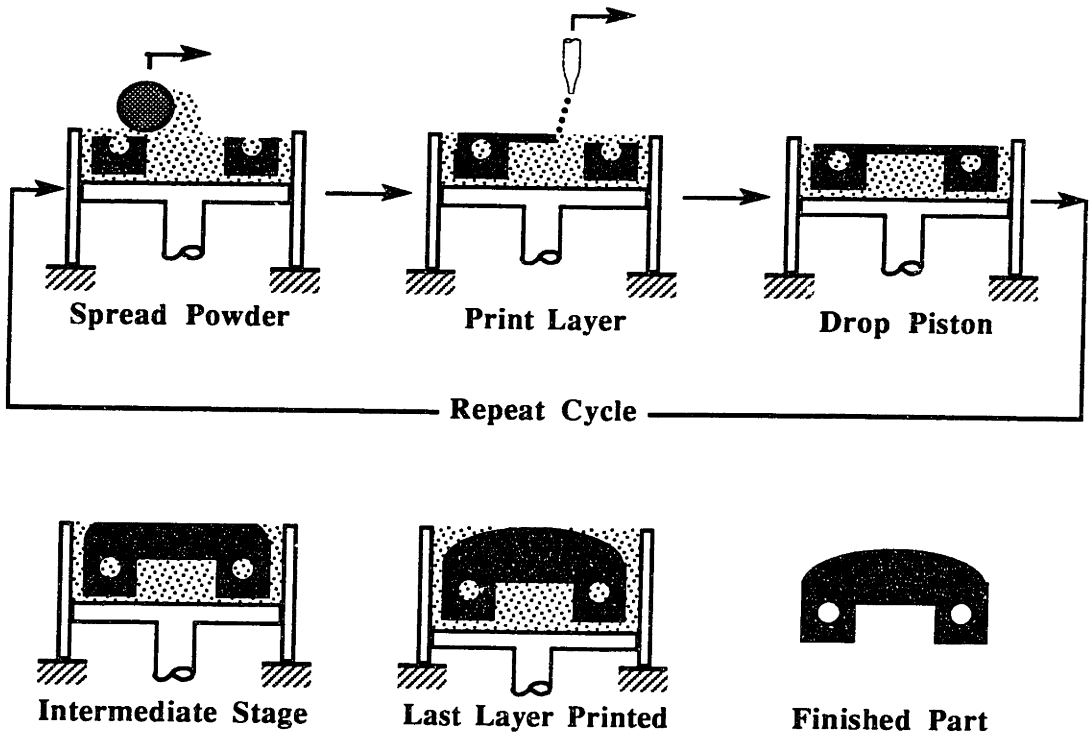

Figure 2.6 Three Dimensional Printing Process Sequence.

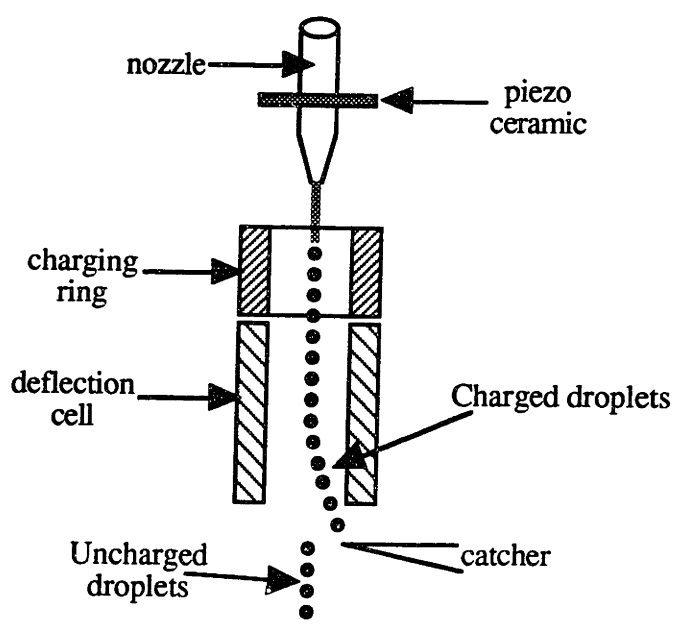

Figure 2.7 Schematic Diagram of a Continuous-Jet Printhead.

droplets continue to fall vertically. Deflected droplets are caught by a metal protrusion, or catcher, at the base of the printhead and prevented from falling into the powder bed. The continuous-jet printhead is illustrated in Figure 2.7.

The printhead raster motion is driven by a positioning system consisting of a linear stepper motor, a lead-screw table and rotary stepper, and a two-axis controller made by DCI (Franklin, MA). The printhead is attached to a carriage which is driven back and forth across the powder bed by the linear stepper motor at speeds up to 2.5 m/s. Typical operational speeds are around 1.65 m/s. The linear stepper motor apparatus, carriage, and printhead constitute the fast axis in the raster pattern. This entire assembly is mounted to the lead-screw table, driven by the rotary stepper motor. The rotary stepper drives the slow axis of the raster by incrementing the position of the printhead with respect to the powder bed between each pass along the fast axis. The minimum step size of the slow axis is 1.3 μm; the standard increment during printing is 175 μm. Both motors are controlled by the DCI-1000 two-axis controller, which can be programmed directly or be governed by an external computer program. Figure 2.8 is a schematic diagram of the 3D Printing hardware.

Powder layer generation is accomplished by spreading powder from one side of the piston using a spreader rod, and is fully automated. A hopper containing the powder supply is located at one side of the powder bed. After a layer is completed and the piston has been lowered, the hopper deposits a pile of powder at the edge of the powder bed. The spreader rod then pushes the powder across the piston, filling the small gap caused by the lowering of the piston and leveling the powder surface. Typically, the rod is counter-rotated during spreading, but it is also capable of press-rolling or no rotation. An electromagnetic shaker is also attached to the spreader rod allowing it to be vibrated transverse to its axis. Under standard conditions, the rod is vibrated in the vertical plane at 400 Hz. A detailed description of powder layer generation techniques and the resulting characteristics of the powder bed are available elsewhere (Lee, 1992).

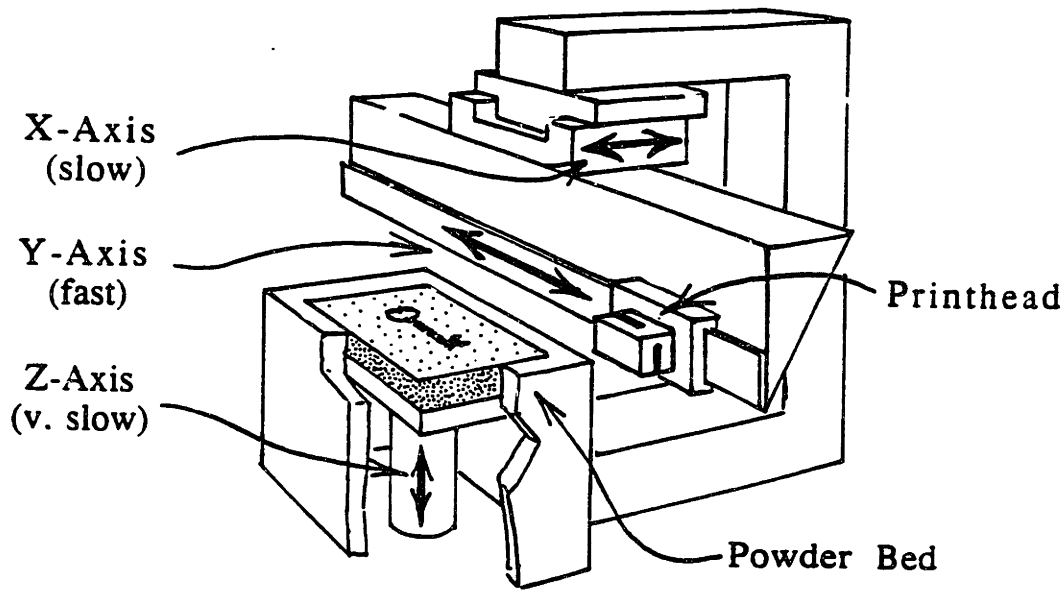

Figure 2.8 Schematic Diagram of the Three Dimensional Printer.

Materials and Applications

Three Dimensional Printing is unique among rapid prototyping technologies in its ability to use almost any material with very few restrictions. Almost any powdered material can be joined with some type of liquid binder. 3D Printing is currently used to make parts from both metal and ceramic powders, but is not limited to these.

The first application for Three Dimensional Printing is the direct manufacture of shells and cores for metal casting. Materials for these parts are aluminum oxide (alumina) powders bound by a colloidal dispersion of amorphous silicon dioxide (colloidal silica). These materials are used to produce a glass-bound refractory material, similar to that used in the investment casting industry (Cima and Sachs, 1991). 3D Printing offers a large lead time reduction in the production of molds for prototype and one-of-a-kind castings. Implementation of Three Dimensional Printing to make ceramic shells and cores has been termed "CAD-Casting" (Sachs, Cima, Bredt, and Curodeau, 1992), following the convention that a casting process is named by how the mold is produced (e.g. sand casting, investment casting, or die casting). Figure 2.9 is a photograph of an integral

shell and core fabricated by 3D Printing. The microstructure of these parts is the focus of this thesis. Important parameters have been found to include powder morphology, powder/binder ballistic and wetting interactions, and powder cohesion, among others (Lauder, Cima, Sachs, and Fan, 1991; Fan, Lauder, Sachs, Cima, 1992).

Silicon carbide powder bound with colloidal silica constitutes a second ceramic materials system used in Three Dimensional Printing. Silicon carbide preforms have been fabricated for use as the reinforcement phase in metal matrix composites (MMCs). 3D Printing removes many of the geometric constraints of traditional ceramics processing, allowing new composite configurations to be tested. MMCs are produced by infiltrating the SiC matrix with molten aluminum under pressure. Both macro-toughened and uniformly reinforced composites have been made by this procedure. Figure 2.10 is a micrograph of the cross section of a metal matrix composite produced using a 3D Printed reinforcement phase.

Metal powders may be used to directly fabricate functional tooling by Three Dimensional Printing (Michaels, 1992). Current work involves binding stainless steel powders using a dispersion of latex particles. In one procedure, the latex binder is burned out following printing and the steel part is sintered. Another method involves infiltrating the porous stainless steel part with a second-phase metal to produce a fully dense metal part. One application demonstrated for these parts is rapid prototypes of injection molding inserts. A photograph of a 3D Printed injection molding insert is shown in Figure 2.11. Other uses of these techniques for metals are under development, and the process is not limited to stainless steel powders.

Several other materials systems and applications are currently under development for use in Three Dimensional Printing. Examples include alumina powder with finely dispersed alumina as a binder for making advanced ceramic components and fabrication of cermets such as tungsten carbide / cobalt components for tooling. Use of alumina/silica parts as porous ceramic materials for hot gas filtration is also being tested

(Alvin, Lippert, and Lane, 1991). Table 2.2 summarizes the 3D Printing material systems and applications.

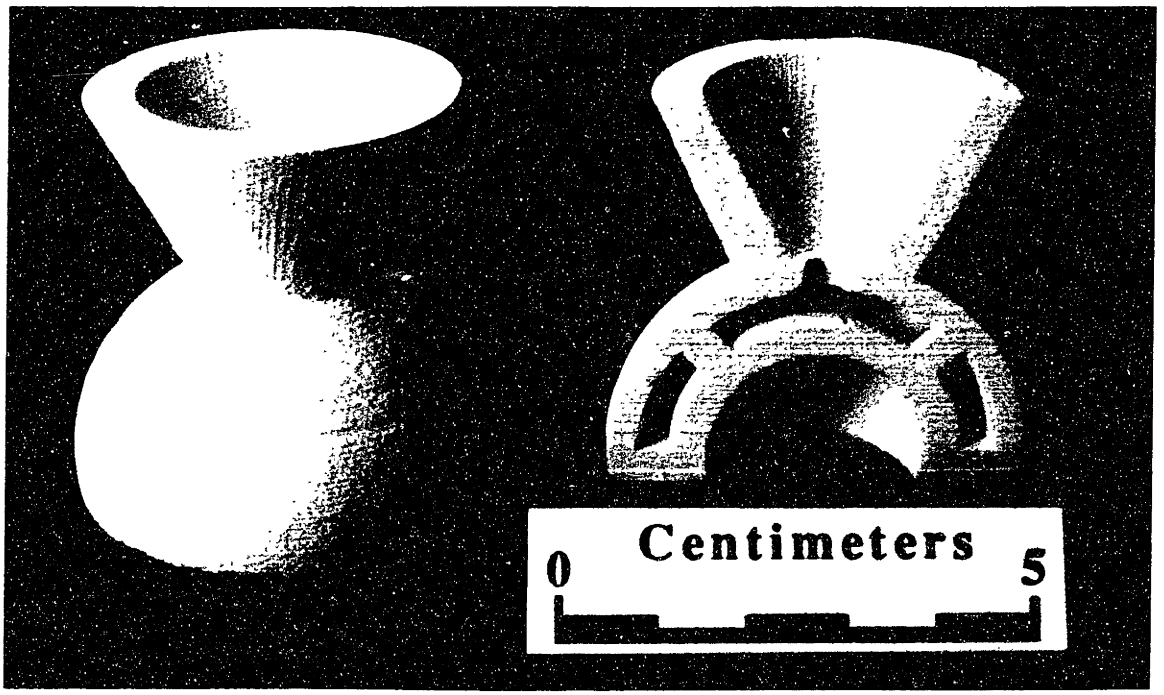

Figure 2.9 Photograph of a complete printed shell for metal casting and a printed cross section of the same part.

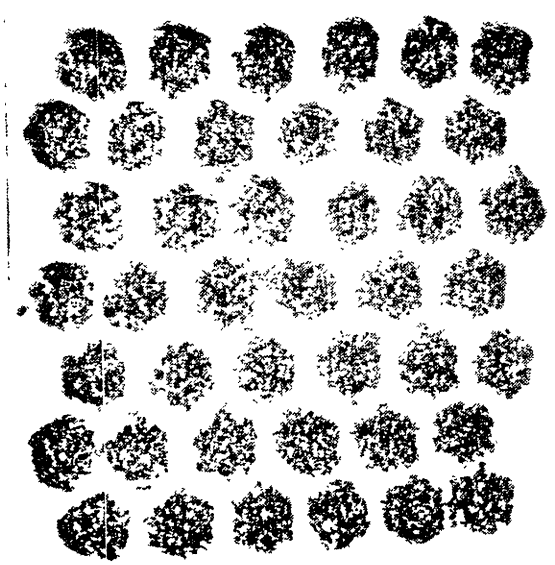

Figure 2.10 Micrograph of a cross section of an Al/SiC composite produced using a 3D Printed reinforcement phase.

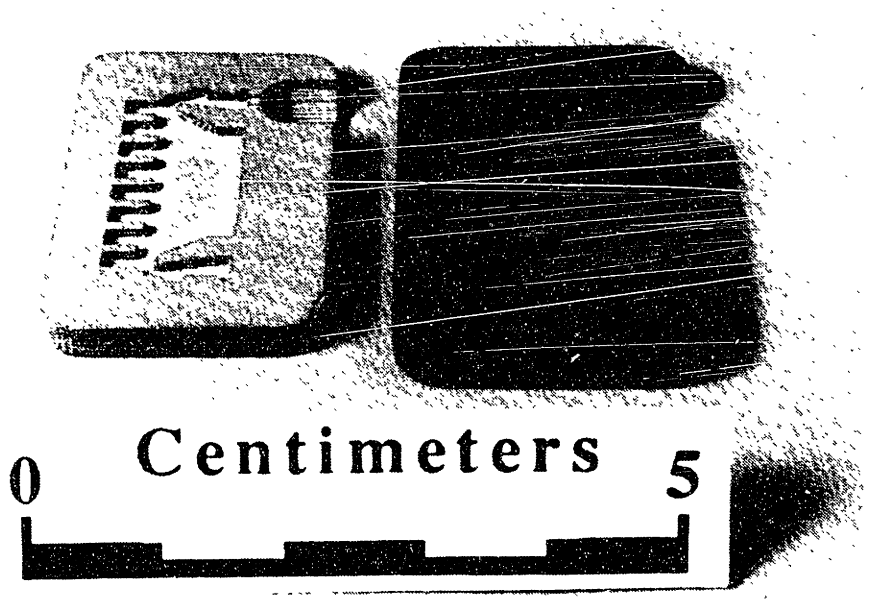

Figure 2.11 Photograph of a stainless steel part for use as an injection molding insert produced by 3D Printing. (Michaels, 1992)

Table 2.2 Three Dimensional Printing Materials and Applications

Powder	Binder	Application
Alumina	Colloidal Silica	Shells and cores for rapid production of metal castings
Alumina, other oxide or non-oxide ceramics	Finely Dispersed Alumina, Zirconia or Silica	Fabrication of advanced ceramic components
Alumina	Colloidal Silica	Porous ceramic materials for hot gas filtration
Silicon Carbide	Colloidal Silica	Preforms for metal matrix composites
Stainless Steel or other metal powders	colloidal latex	Sintered or infiltrated metal parts for injection molding tooling
Tungsten Carbide - Cobalt	under development	Cermet parts for rapid tooling

3. EXPERIMENTAL PROCEDURE

3.1 Strategy

Microstructural characterization, the main goal of this work, was carried out by systematically studying the most basic features of a 3D Printed part and gradually adding more complexity. This was accomplished in several stages. First, the materials to be used for the study were chosen and in some cases fabricated. Using these materials, experiments were carried out to trace development of the microstructure from its smallest units to a complete part. Studying the interaction and resulting features of a single binder droplet contacting the powder bed was the first of four main sets of experiments. The second set involved investigation of single lines formed by a train of droplets. Next, several layers were printed sequentially each containing a single line in the same location. This formed a vertical wall with a thickness of one line width. The final set of experiments involved printing groups of lines in each layer to build bars that had a thickness of several line widths.

3.2 Materials

The ceramic material system was the primary focus of this study; specifically alumina powders and a colloidal silica binder. These materials are used to produce glass-bonded refractories for metals casting, and were the first materials studied extensively for use with 3D Printing (Esterman, 1990).

Binder

The binder used for these experiments was a colloidal silica sold under the name Nyacol 830. The binder contains 30% amorphous silica by weight. The silica is in the form of 8 nm spherical particles, and is suspended in a basic aqueous medium. The binder has a pH of approximately 10.5, and becomes unstable at lower pH. A 25%

aqueous solution of tetramethylammonium hydroxide is added to the colloidal silica in the proportion of 10% by weight. Addition of quaternary ammonium bases such as tetramethylammonium hydroxide have been shown to reduce the viscosity of colloidal silica and stabilize it against flocculation (Iler, 1979). These properties aid the passage of the binder through the small orifice during printing. On drying, the sol becomes a silica gel that binds the alumina particles together and gives them limited green strength.

Two characterization experiments were carried out on the binder. One involved titration of the binder to determine the amount of acid necessary to bring on gelation due to instability at low pH. Flocculation of colloids due to changes in pH is a well understood phenomenon predicted by the DLVO theory (Shaw, 1966), but experiments were necessary in this case to determine the concentrations of specific acids required to flocculate the treated binder. Two different acids were used: an aqueous solution of citric acid, and an aqueous solution of polyacrylic acid. The titration was done by hand with a buret, and pH was measured using pH testing paper and a color chart. This method was used due to the difficulty of cleaning the probes of a pH meter after the binder gelled around it, and because the resolution of 0.2 to 0.5 pH units was sufficient to estimate the concentration of acid.

A second set of binder experiments was conducted to measure the surface tension of the treated binder. This was done using a Wilhelmy plate apparatus calibrated against published values for water-ethanol mixtures. Surface tension measurements were conducted for several levels of tetramethylammonium hydroxide concentration between 0% and 10%.

Powder

Four different alumina powders were studied. Effects on the microstructure of printed parts were analyzed with attention to the size, morphology, and packing density of each powder. The powders selected for these studies were Norton 38 Alundum Flour,

Norton 30 μm Electronic Grade, ICD 10 μm Alunabeads, and a spray dried alumina powder. Characterization experiments were conducted for each powder.

Norton 38 Alundum Flour is a 99.5% pure Al_2O_3 powder produced by the Norton Company (Waltham, MA). It is manufactured by comminution from large particles and has a irregular faceted gravel-like appearance. The particle size is less than 49 μm, achieved by sieving out coarse particles through a 325 mesh sieve. The size distribution is wide, and some fines are present. Figure 3.1 shows a micrograph of a typical sample of Norton 38 Alundum Flour.

Norton 30 μm Electronic Grade is a 99.99% pure Al_2O_3 powder also made by the Norton Company. It is produced by a chemical method and consists of hexagonal platelets. The average particle diameter is 30 μm. The particle size distribution is fairly narrow, with no fines present. Figure 3.2 is a micrograph of a sample of this powder.

ICD Alunabeads CB-A10 is a spherical Al_2O_3 powder produced by Showadenko Corporation (Japan) and distributed in North America by the ICD Group (Lyndhurst, NJ). Alunabeads are produced by plasma torch spheroidization of alumina particles, and have an average particle size of 10 μm. Some fine spherical particles are included. Figure 3.3 is a micrograph of the 10 μm spherical alumina.

The spray dried alumina powder was produced from Reynolds RC172 sub-micron alumina using a laboratory scale spray drier. The binder used was 2% polyacrylic acid by weight. The final product was a porous spherical powder with a typical spray dried morphology. The average particle size was determined to be between 10 μm and 20 μm by microscopic examination, with very few loose sub-micron particles present. Figure 3.4 show a micrograph of a typical sample of the spray dried powder. A detailed description of the spray drying procedures and formulations is given in Appendix A.

Two characterization experiments were conducted on each powder. Helium pychnometer measurements were made to determine the skeletal density of the powder

Figure 3.1 Micrograph of a typical sample of Norton 325 mesh alumina powder.

Figure 3.2 Micrograph of a typical sample of Norton 30 μm Electronic Grade alumina.

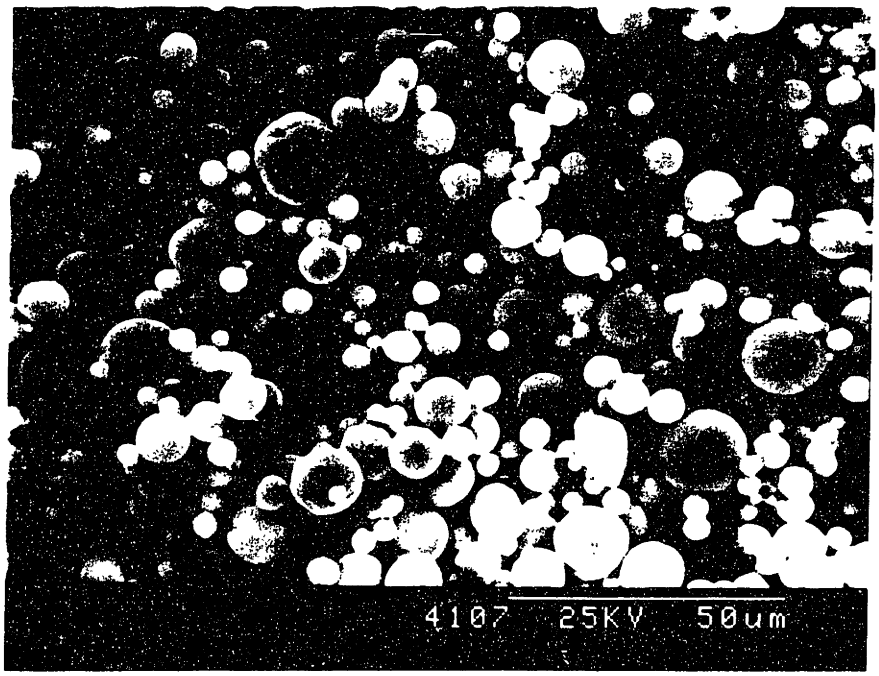

Figure 3.3 Micrograph of a typical sample of ICD Alunabeads 10 μm spherical alumina.

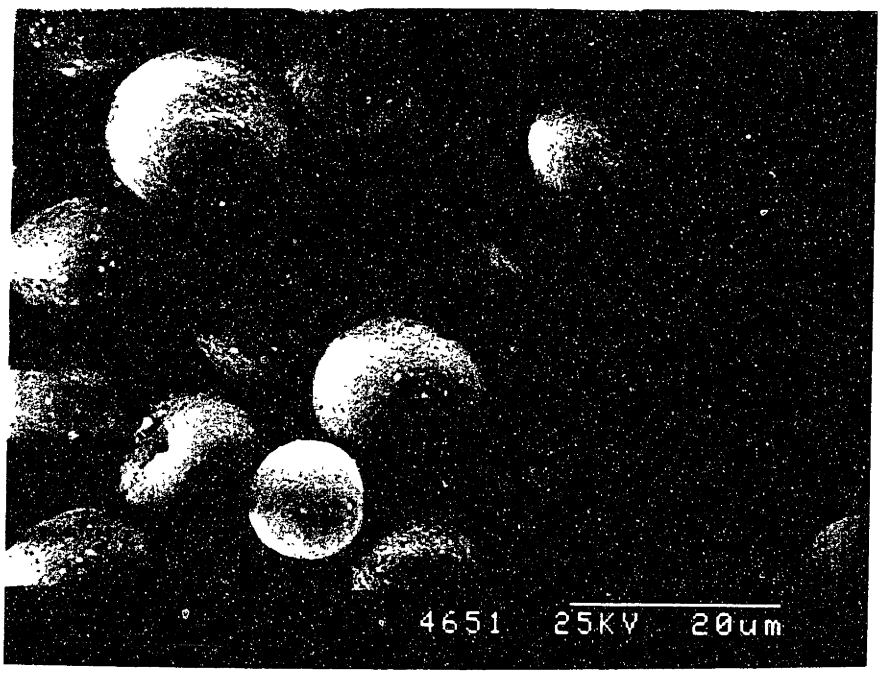

Figure 3.4 Micrograph of a typical sample of the in-house spray dried powder.

using a Quantochrome BET / Pychnometer apparatus. Pychnometer measurement were done with a sample size of approximately 15 g and a cell volume of 30 cc. Mercury porosimetry, using a Micromeritics Autopore II machine, was used to measure pore size distributions and bulk density of the powders. Pressures up to 216.5 MPa (30,000 psi) were used to infiltrate mercury into the powders. Sample sizes were approximately one gram in a penetrometer with a 3 ml volume. Packing density measurements for 3D Printing as-spread conditions are also available (Lee, 1992).

3.3 Sample Preparation

All samples were made using the Three Dimensional Printing apparatus at MIT under laboratory conditions. Usual printing procedures were followed, including adjustment of the flow rate, piezo frequency, deflection cell voltage, and spreading of foundation layers. Binder flow rates were approximately 1.2 cc/min for all experiments. Other parameters were adjusted on a day-to-day basis to optimize nozzle performance. Printing patterns, layer thicknesses, spreading sequence, and line spacings varied from experiment to experiment and will be described for each kind of sample.

3.4 Firing Schedule

After printing was completed, samples were removed from the powder box while still in the powder bed. The samples were dried overnight in an oven at 100° C, and then taken to the furnace for firing. Limited microstructural analysis was carried out on samples in the green state. Samples were fired in the powder at 900° C for two hours then allowed to cool to room temperature before removal. This schedule causes formation of a silica glass which bonds the alumina particles, but does not cause sintering. Shrinkages due to the heat treatment are less than 0.4% (Esterman, 1990). Figure 3.5 is a diagram of the 3D Printing firing schedule. Excess powder was removed after firing. The method of removing excess powder varied, depending on sample type.

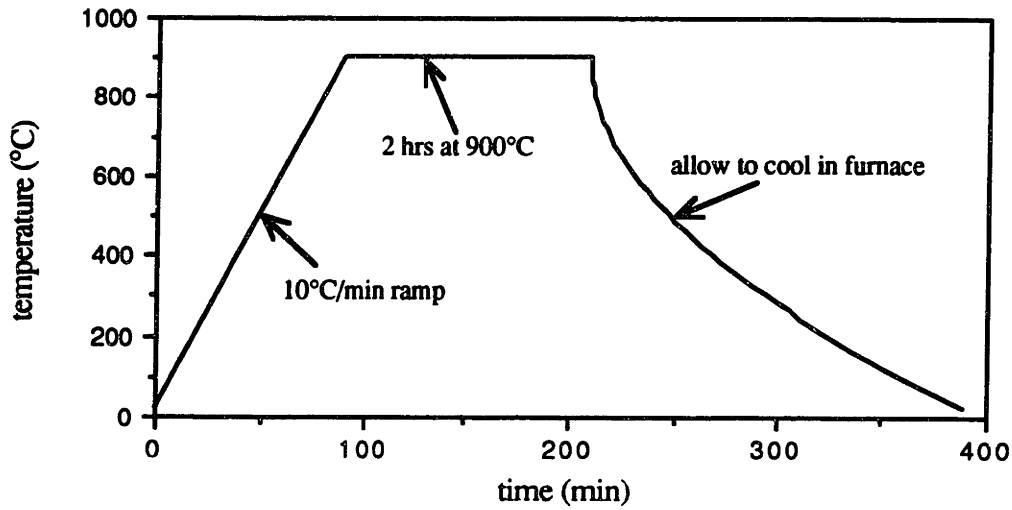

Figure 3.5 3D Printing Firing Schedule.

3.5 Primitives

The simplest structure that can be made by 3D Printing is one which results from the contact of a single binder droplet with the powder bed. Accordingly, these were the first types of samples to be made and were termed "primitives." A detailed study of primitives was conducted in order to identify the microscopic processes that influence 3D Printing at the most basic level.

Preparation

Samples were made by two methods. The first used a syringe and a 16 gage needle to spray binder into a powder bed. This method was useful because it was possible to produce large numbers of primitives quickly and the size of the drops was large enough to observe the absorption process with the naked eye, but had the drawback that it was difficult to accurately meter the size of each binder drop. The smallest droplets produced using this method were one to two orders of magnitude larger than those

produced by the Three Dimensional Printing machine. The resulting primitives were irregular in size and shape due to the difference in initial droplet sizes, but observations of primitive formation were made that may be qualitatively similar to processes occurring in 3D Printing.

The second method of making primitives was by using the 3D Printing machine. A special circuit was designed to drive the charging cell instead of the usual data from a .TDP file. This circuit allowed only one droplet out of every 32 to remain uncharged and strike the powder bed. Thus, neighboring droplets along a line were separated by almost 0.8 mm (0.031 in.) and were to far apart to stitch together. For these experiments, a layer thickness of 380 μm and a line separation of 780 μm were used. Complete coverage of the 90 x 90 mm powder bed produced more than 10,000 primitives per layer. In most cases, at least 20 layers were printed. After printing, the powder was carefully scooped out of the piston and fired according to the normal schedule. The powder was then passed through several sieves of different mesh sizes to separate the primitives from the unbound powder.

The single droplet generating circuit was also modified to produce continuous trains of 8 continuous uncharged droplets separated by 24 charged droplets. This produced 8-drop primitives, which were used to examine the stitching of small numbers of droplets. The line spacing and layer height used for these experiments was the same as for the single drop primitives discussed above. As with the single drop primitives, 8-drop primitives were sufficiently distant from one another to prevent stitching. Firing and removal from the powder bed was also accomplished by using the standard firing schedule and then sieving to separate the printed areas from the unbound powder for these samples.

Process Parameters

The main variable examined in the primitive formation experiments was that of powder morphology. Each of the four different alumina powders was used to produce single drop primitive. 8-drop primitives were made from the Norton 30 μm alumina and from the in-house spray dried powder. The different powder morphologies and sizes caused slight variations in primitive microstructure, making it possible to deduce the important interactions between the powder and binder in 3D Printing.

Another variable of interest was the packing density of the powder bed. Packing density is expected to show a positive correlation with the cohesive strength of the powder. Therefore, as the packing density increases particle rearrangement due to powder/binder interactions should become more difficult. The packing density of the powder bed was only measured directly in a few cases. This was performed by careful measurement of the piston volume and the powder mass. These measurements proved to be highly reproducible. More often, however, the packing density of the powder bed was taken to be that found in other experiments in which a database of packing measurements was created for several spreading conditions (Lee, 1992). Because of this, spreading conditions were carefully chosen for each set of experiments to correspond with standard conditions. The most common spreading sequence used was to drop the piston 2 layer thicknesses, spread using counter-rotation and vibration (400 Hz) of the spreader rod, raise the piston one layer thickness (for a net drop of one layer thickness), then counter-roll the rod back across the bed to remove excess powder. Powder packing densities are given in Table 3.1.

Table 3.1 Powder Packing Densities

Powder	Density (g/cc)	% of theoretical
Norton 325 Mesh Alumina	1.39	35
Norton 30 μm Electronic Alumina	1.91	48
ICD 10 μm Alunabeads	1.90	48
Spray Dried Alumina	1.10	29

Experiments

Three sets of experiments were used to characterize primitives. Density measurements conducted by Helium Pychnometry were always done first on the entire batch of fired primitives for a particular number of droplets, powder, and packing density combination. This measurement was done first because it requires the largest possible sample size and is non-intrusive and non-destructive. The primitives were accurately weighed on an analytical balance to an accuracy of ±0.2 mg. The sample size varied between 2 and 4 g depending on the amount of primitives obtained. The samples were then placed in the pychnometer cell using a cell volume reduced to 20.00 ml by addition of a calibrated dummy plug. The cell was sealed and purged for one hour by low pressure helium flow. Pychnometer measurements were then taken using pressures of approximately 140 kPa (20 psi). Repeated measurements were taken until three values for sample volume agreed within 1%; this usually required 5 runs. The final three runs were averaged to and used to calculate the skeletal density of the primitives. This information could then be used to calculate primitive composition, since the density of both the silica and the alumina powder were known.

A small sample of each set of primitives was taken for microscopic analysis using a Scanning Electron Microscope. A few milligrams of primitives were affixed to an SEM stub using adhesive press tabs, and were then gold coated for 45 s in a Denton sputter coater. Samples were observed using a Hitachi Scanning Electron Microscope with a beam energy of either 20 or 25 kV. Photographs were taken using the attached Polaroid system.

The remaining primitives were analyzed by Mercury Porosimetry to obtain a pore size distribution and a measurement of bulk density. Again, primitives were weighed using an analytical balance with a typical sample size of one gram. The penetrometers used were the powder-type with a raised stem and had a sample volume of 3 ml. After the sample chamber was evacuated to a pressure of 50 μm of Hg, the chamber was filled

with mercury at a pressure of 21.6 kPa (3 psi). In some cases, this was not sufficient to completely infiltrate the inter-primitive cavities and corrections had to be made to the data later. Infiltration volume was measured at 185 pressures up to a maximum of 216.5 MPa (30,000 psi) using a Micromeritics Autopore II. In most cases, two porosimetry runs were conducted but for some sample types only enough primitives for one run were obtained. Mercury porosimetry data was used to determine pore sizes and void fractions in primitives.

3.6 Lines

A line is the structure resulting from one pass of the printhead over the powder bed, and is the simplest level of control in the raster scan pattern. Single lines and sets of adjacent lines were printed to study the next higher level of complexity than primitives in 3D Printed parts. Examination of lines was used to examine stitching of the individual droplets of binder and to observe the effects of the ballistic interaction of droplets with the powder bed. Unlike primitives, lines were very fragile and could not easily be removed from the powder bed intact. Line experiments were conducted while the sample remained in the bed for this reason.

Preparation

Lines were printed in a modified powder bed to allow microscopic examination without the necessity of removing excess powder. Because lines were examined *in-situ* , the surrounding powder bed could also be studied to determine the effects of ballistic interactions between the binder droplets and the powder. *In-situ* observations were accomplished by printing lines into a modified powder bed made from a standard SEM stub with a washer glued on top. The washer provided 6 mm high walls encircling the top of the stub. Powder was spread by hand in this area.

Line experiments were limited by the fragility of the samples, therefore, only one set of experiments was performed. The powder used was Norton 325 mesh alumina. Each sample contained 5 printed lines: the first printed alone, then a set of 2 adjacent lines separated by 89 μm, then another set of 2 adjacent lines separated by 178 μm (the standard 3D Printing line spacing). Figure 3.6 is a schematic diagram of the sample holder and the print pattern. The sample holder was clamped at the same distance from

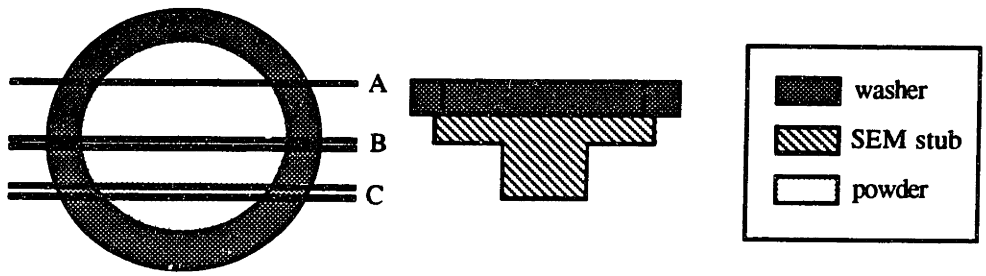

TOP SIDE

Figure 3.6 Schematic of line sample holder and print pattern. Top and side views of the sample holder are shown. The letters A, B, and C next to the heavy lines indicate printed lines. A is a single line; B is two adjacent lines separated by 89 μm; C is two adjacent lines separated by 178 μm.

the printhead as is normal for the powder surface during printing. After printing, some samples were sealed in a desiccator half filled with warm water in an attempt to prevent them from drying out. Other samples were placed in an oven at 100 C for an overnight cure.

Experiments

Microscopic examination was the only analytical technique used on line samples due to the constraint of leaving them in the powder bed. The samples that were placed in the high humidity chamber were immediately taken for observation in an Environmental Scanning Electron Microscope (ESEM). The samples were placed in the ESEM, manufactured by ElectroScan (Wilmington, MA), within 15 minutes of printing. Samples were observed under low to medium magnification for effects of drying. The

images were recorded on SVHS video tape. The samples which were cured overnight were observed using an SEM. After first marking the washer to preserve orientation, the same gold coating and observation procedures were used as for the primitives. Care was taken not to disturb the lose powder bed.

3.7 Walls

Walls are made up of a line or a group of adjacent lines that is printed into several consecutive layers to build a long, tall, thin rectangular solid. Sets of walls that are only a single line width thick demonstrate the stitching of lines in the vertical direction. Walls that have thicknesses of more than one line width require stitching in both the horizontal and vertical planes. Multiple line width walls contain all the structural features of a complete 3D Printed part, but are small and easy to study. Wall samples were used as a simple model of 3D Printed parts to complete the study of microstructural development from primitives to complete components.

Preparation

A wall was formed by repeating the process of printing a single line of binder (or several adjacent lines) across the powder bed, then spreading a fresh layer of powder and printing another line directly on top of the first. Two different print patterns were used to produce wall samples; one for single line width walls and another for multiple line width walls.

A previous study used single line walls to study the effect of binder content on part structure (Curodeau, 1990). This was accomplished by varying the traverse speed of the printhead while keeping the binder flow rate constant. Variations in wall thickness were measured and found to correlate positively with decreasing printhead velocity. An interesting observation was that at high binder contents, the void space in the powder bed reach saturation and walls became very wide. It was also noticed that the bottom or side

surfaces of many parts had unwanted particles attached, due to percolation of excess binder. This phenomenon was termed bleeding, and was an issue for dimensional control of printed parts.

The bleeding problem was easily corrected by addition of a powdered acid to the alumina powder. The presence of the acid lowered the pH of the binder to an unstable region and caused gelation. This served to arrest the percolation of the binder. Microstructural effects of acid additives to the powder bed were studied in the first phase of wall experiments. For these experiments, the print pattern used was the same one that Curodeau used for binder content experiments. This pattern produced 9 single line width walls, each printed at a different printhead speed varying between 50.8 cm/s and 152.4 cm/s. A diagram of the print pattern is shown in Figure 3.7. Each set of walls was printed to a height of 0.63 cm, using a layer height of either 125 μm or 250 μm. The printhead speed was changed between each pass using the DCI motion controller directly, instead of by using the standard .TDP software.

The second group of wall experiments involved printing multiple line width walls. These samples were used to study the microstructural arrangement of all the elements of 3D Printed parts from primitives to stitched planes. Walls were printed onto an alumina substrate using the standard line spacing of 175 μm and the standard layer height, also 175 μm. Normal printing procedures were followed for set up, and the binder flow rate was adjusted to 1.2 cc/min ± 10%. Each set of walls contained a single line width wall and two walls each of 2, 3, 4, and 5 line widths for a total of 9 walls per sample. For each pair of multiple line walls, one was printed with an extra one or two line ridge running along the top. The ridges were included to study particle arrangement at inside and outside corners. Walls were fired using the standard 3D Printing schedule. Figure 3.8 is a schematic diagram of the multiple line width walls print pattern; Figure 3.9 is a side view of the wall construction.

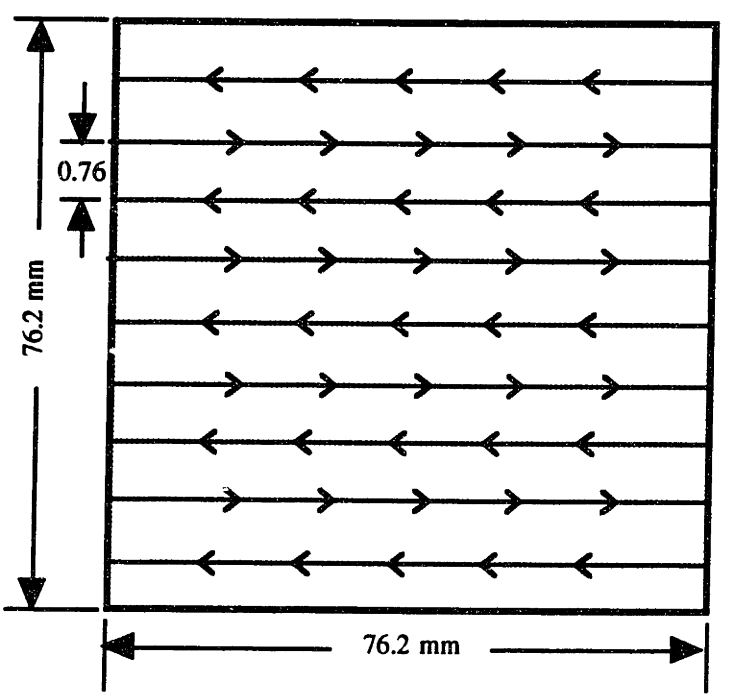

wall #	speed (cm/s)
1	50.8
2	63.5
3	76.2
4	88.9
5	101.6
6	114.3
7	127.0
8	139.7
9	152.4

Figure 3.7 Schematic diagram of print pattern for single line walls. Walls are represented by horizontal lines crossing the powder bed; arrows indicate the direction of printhead motion. Each of the 9 walls was printed with a different printhead velocity, given at the right of the diagram.

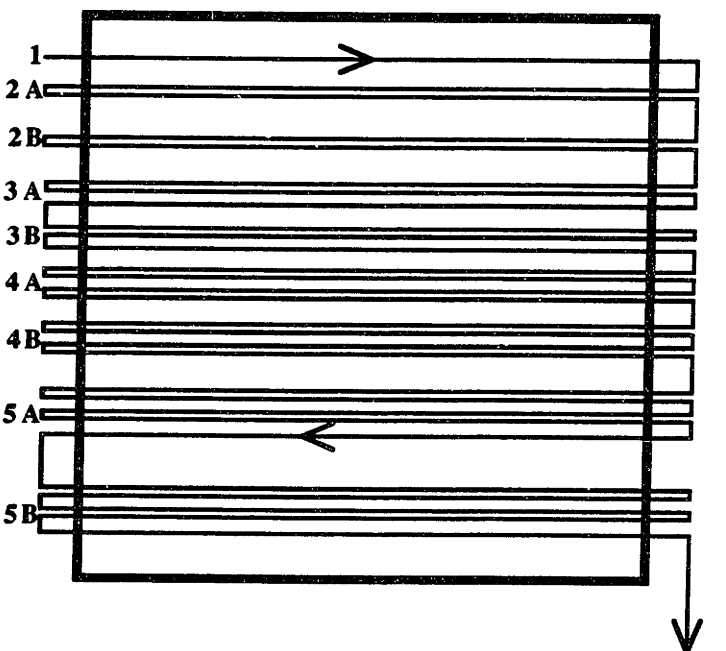

Figure 3.8 Schematic of multiple walls printhead pattern. Each wall was given a code consisting of a number followed by a letter. The number signifies the thickness of the wall in line widths. The letter is either A or B. An A means that the wall has a flat top surface, while a B means that a ridge is present. Wall 5B was had the additional feature

of a small notch halfway up its front side. The sequence of printing followed the order 1, 2A, 2B, 3A, 3B, 4A, 4B, 5A, 5B. Arrows indicate the direction of printhead motion.

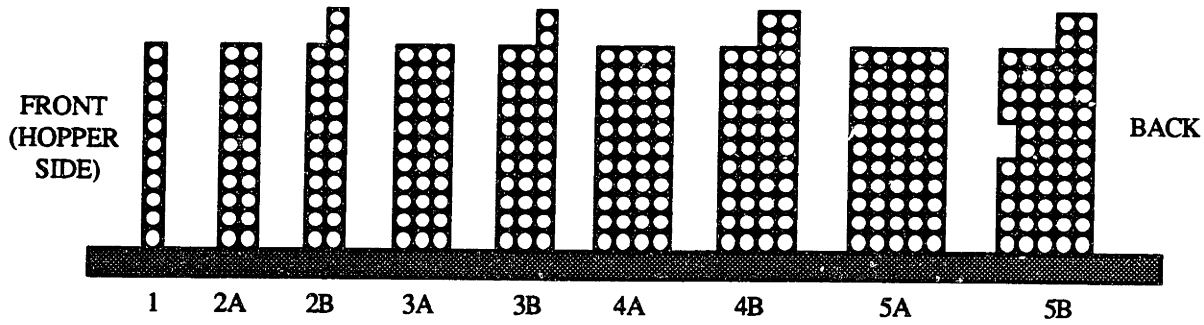

Figure 3.9 Side view of a set of walls, with the fast axis normal to plane of diagram. Walls were printed sequentially from 1 to 5B. B walls have an extra ridge on their top surfaces, always at the back side (the last side to be printed) of the wall.

Process Parameters

The goal of the single line width wall experiments was to study the effect of an acid additive on binder gelation. This was accomplished by printing walls under various conditions and measuring their thickness. Parameters varied were binder content per unit volume, acid type, and acid concentration. Binder content was controlled by two methods: printhead velocity and layer thickness. With a constant flow rate, a slower printhead velocity deposits more binder into a given part volume. Layer thickness determines the volume of powder available to absorb the binder for each printed line.

Acids were chosen based on three criteria: they had to be fairly strong to allow the use of low concentrations, they had to be water soluble, and it was advantageous if they would tend to act as a binder to improve part green strength. The two acids selected for these experiments were citric acid and polyacrylic acid. Both satisfy the first two criteria; polyacrylic acid also satisfies the third because it is a polymer and is occasionally used as a binder in ceramics processing. The concentrations used were 0.2% and 2% acid by weight mixed in to the alumina powder. The values for concentration were selected using the results of the binder titration experiments. A set of walls was also printed containing no additive as a control. Citric acid powder was prepared by grinding

and sieving the acid until it had a particle size approximately that of the alumina, then mixing on a ball mill. Polyacrylic acid powder was made by mixing the alumina with an aqueous acid solution to form a paste, then drying and grinding the paste until the original particle size was regained. The powder used for all powder additive experiments was Norton 325 mesh alumina.

Multiple line walls were printed with the goal of structural analysis. The main variables in this case were the number of lines per wall, the presence of extra surfaces, and the type of powder. The print pattern discussed above described the different wall thicknesses printed. The presence of ridges on the top surface of some walls added and inside corner and sharp geometry change for studying the structural formation of 3D Printed parts. Three different powders were used for wall experiments. The Norton 325 mesh alumina and the ICD spherical alumina powder were both used to print sets of walls. The in-house spray dried powder was also used to print walls using a different print pattern which produced only 5- and 15-line thick walls. In addition, 325 mesh walls were printed using both citric acid and polyacrylic acid additives.

Experiments

Experimental analysis of walls was similar to that of primitives, with two additions. The thickness of single line walls was measured using a stereo microscope with a calibrated scale in one eyepiece. Wall thickness was measured at the second layer from the top, and 3 measurements were taken along the length of the wall. Flow rate data was used to determine the binder volume per unit line length of each wall.

Microstructural observation was done for both single and multiple line width walls. Wall surfaces were prepared for observation by gold coating a section of a specimen and mounting it on an SEM stub. Electron microscope techniques were the same as described for primitives. In addition to surface observations, walls were also viewed in cross section. Several wall specimens were potted in epoxy while standing on

end. The samples were then ground and polished to reveal a cross section perpendicular to the fast axis for SEM observation.

The final set of experiments consisted of a limited number of porosimeter and helium pychnometer measurements of wall specimens. Complete walls were broken up into sections for these experiments, but the wall geometry remained intact. Procedures used for the walls were similar to those described for primitives.

4. OBSERVATIONS

4.1 Primitives

SEM Observations

Single drop primitives, regardless of the powder used, were found to be roughly spherical in shape. Primitives made by the Three Dimensional Printing machine had diameters between 150 and 200 μm. Primitives made by the syringe method were also spherical, although a wide base of agglomerated powder was often present where binder had leaked out of the main ball during formation. The figures on the next several pages are examples of typical primitives: Figures 4.1 and 4.2 are primitives made from 325 mesh alumina, Figures 4.3 and 4.4 are 30 μm powder, Figures 4.5 and 4.6 are spray dried powder, and Figures 4.7 and 4.8 are spherical alumina powder.

Syringe drop primitives were also examined in cross section using both electron and optical microscopes. Transmissive and reflective light sources were used simultaneously for the optical microscopy. Using two light sources allowed viewing of both the exposed cross section and the shadow of any larger sections still embedded in the epoxy mount. Figures 4.9 and 4.10 show typical syringe drop primitives. Figure 4.11 is a scanning electron micrograph of a cross section through a syringe drop primitive. Figure 4.12 is an optical micrograph of the same sample at a lower magnification. Only a very small section of shadow is visible around the primitive, indicating that it has been sectioned through its central plane.

High magnification observation of primitives reveals how the particles are bound by the silica. Figure 4.13 is a scanning electron micrograph of the surface of a 325 mesh single drop primitive. The smooth silica glass can be clearly seen forming bridges between alumina particles, and also coating the particles. The glass shows many cracks, typical of a silica gel that has been dried and fired. Figure 4.14 is a micrograph of the surface of a spray dried primitive. In this case, the silica bridges between particles are

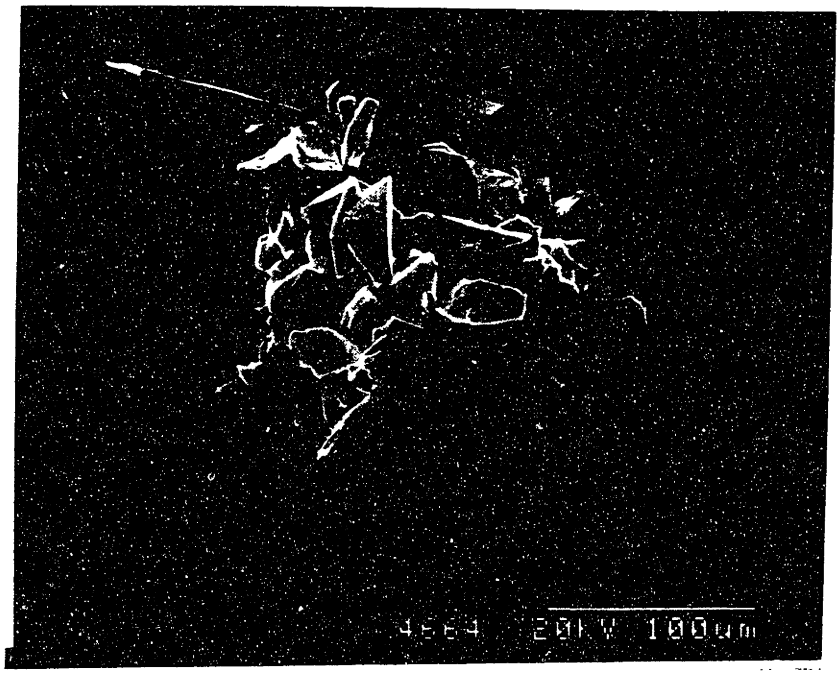

Figure 4.1 Micrograph of a single drop primitive made from Norton 325 mesh alumina.

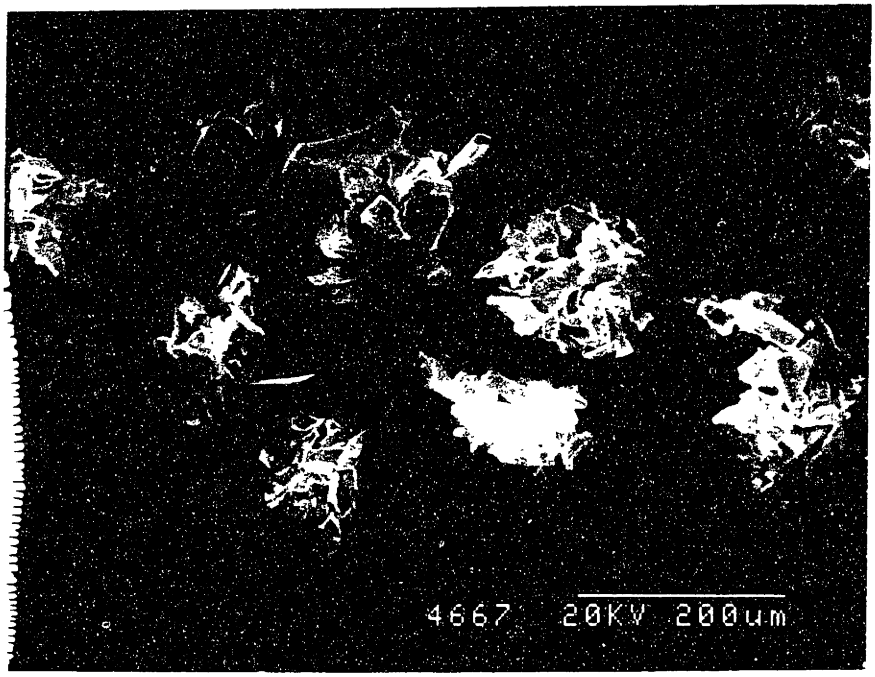

Figure 4.2 Micrograph showing several 325 mesh alumina primitives.

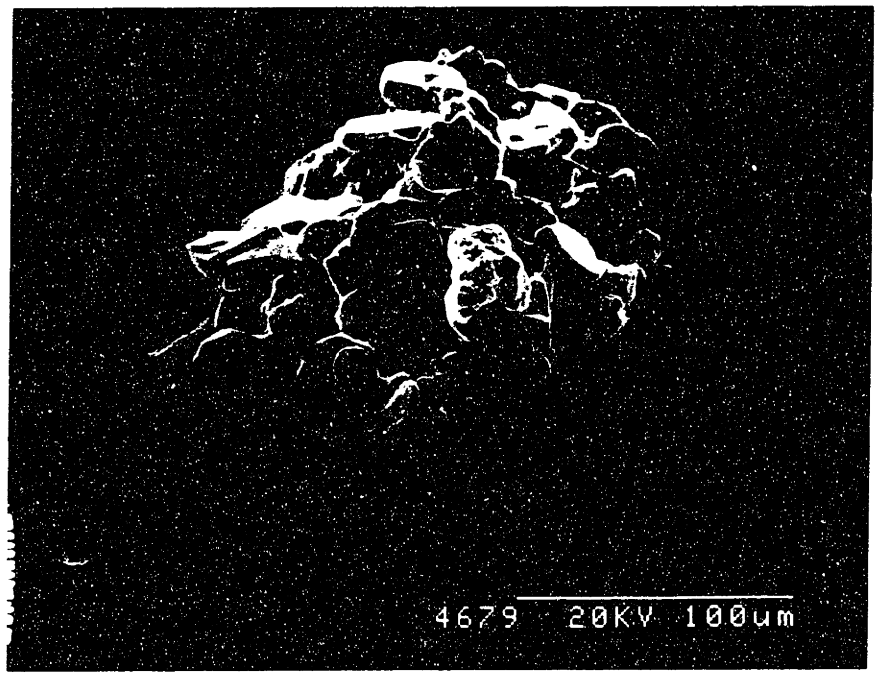

Figure 4.3 Micrograph of a primitive made from Norton 30 μm alumina powder.

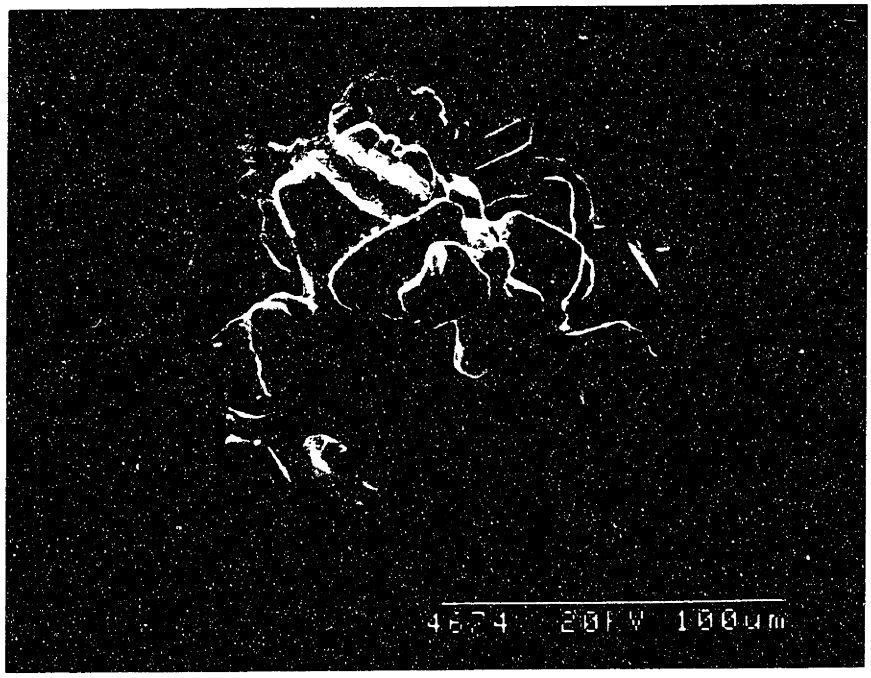

Figure 4.4 Micrograph of a primitive made from Norton 30 μm alumina powder.

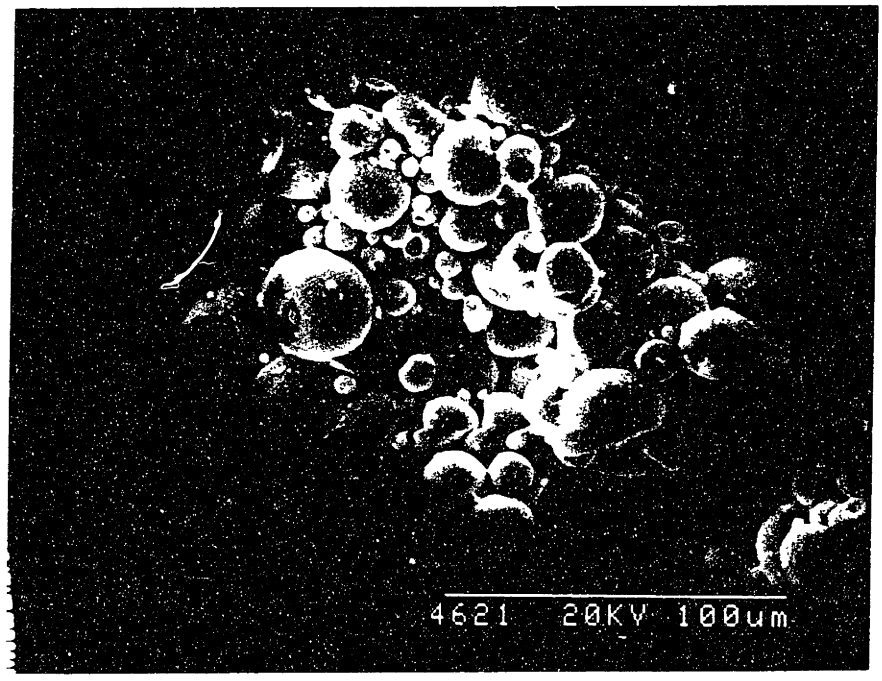

Figure 4.5 Micrograph of a single drop primitive made from the in-house spray dried alumina powder.

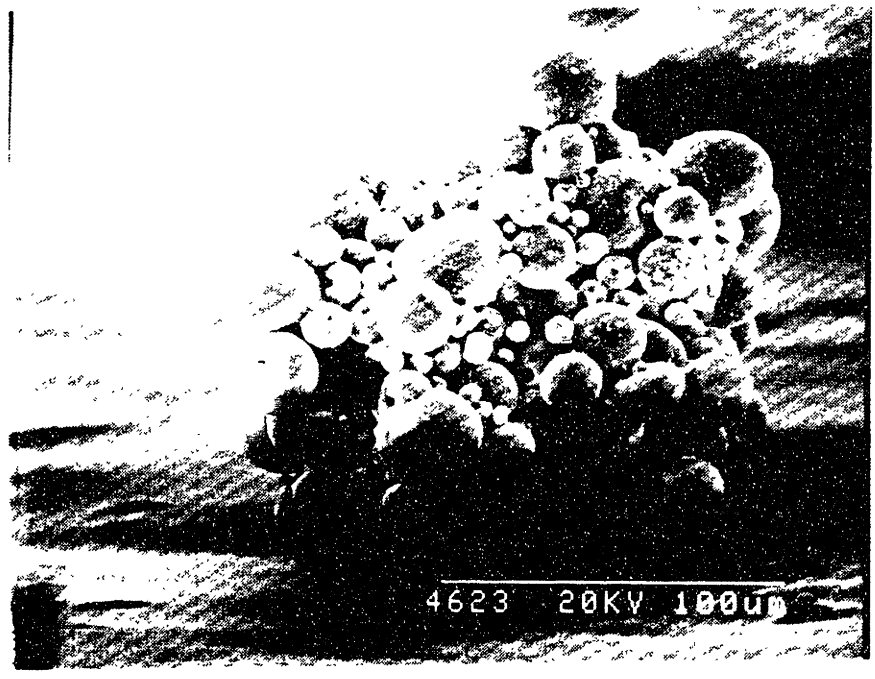

Figure 4.6 Micrograph of a single drop primitive made from the in-house spray dried alumina powder.

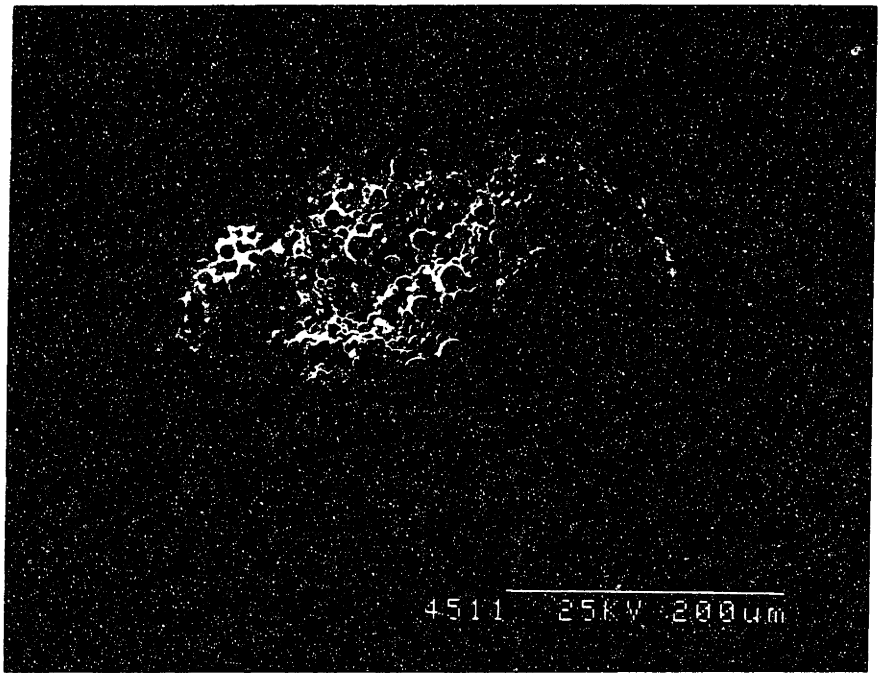

Figure 4.7 Micrograph of a single drop primitive made from the ICD spherical alumina.

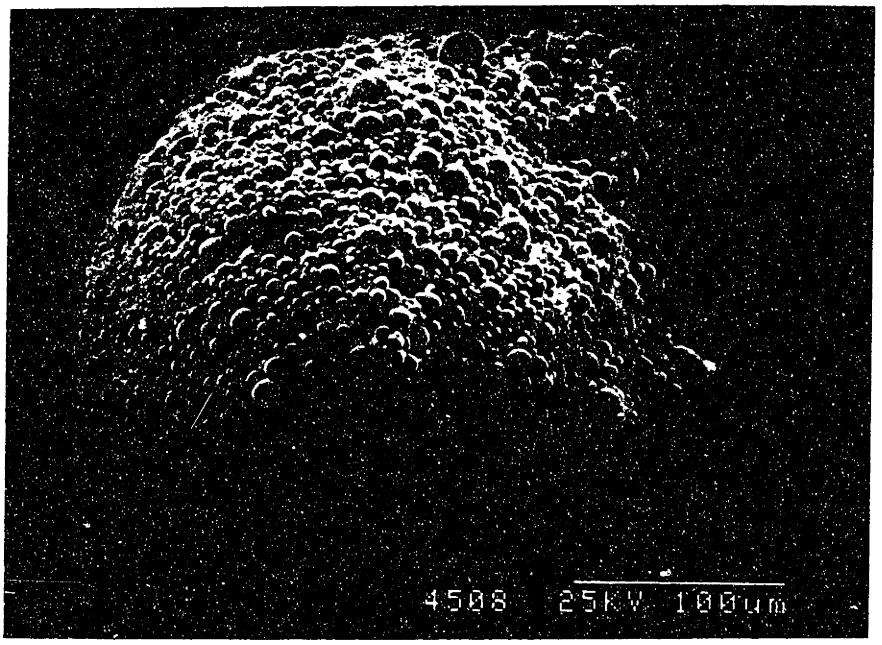

Figure 4.8 Micrograph of a single drop primitive made from the ICD spherical alumina.

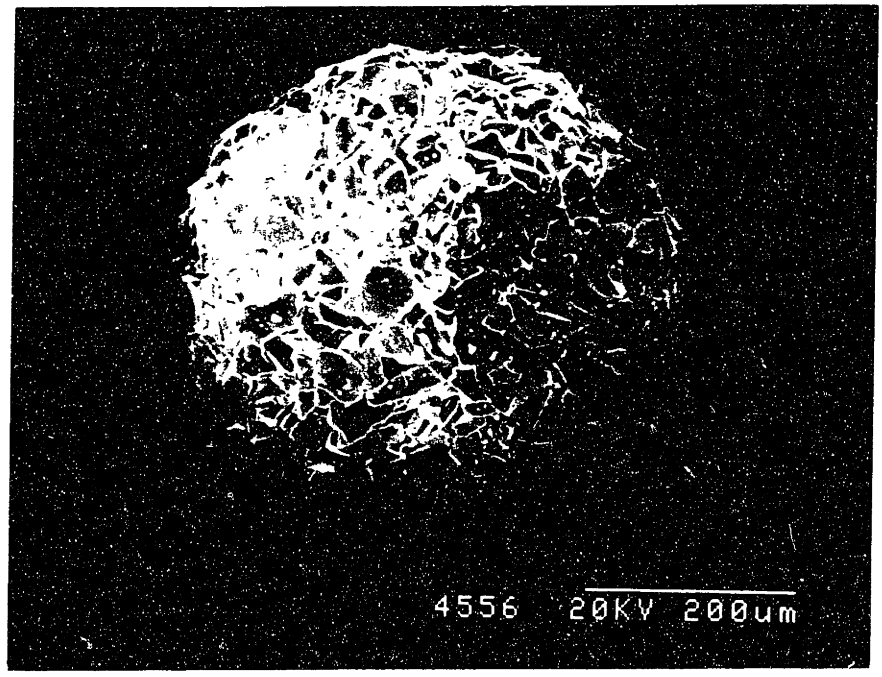

Figure 4.9 Micrograph of a 325 mesh primitive made by the syringe method.

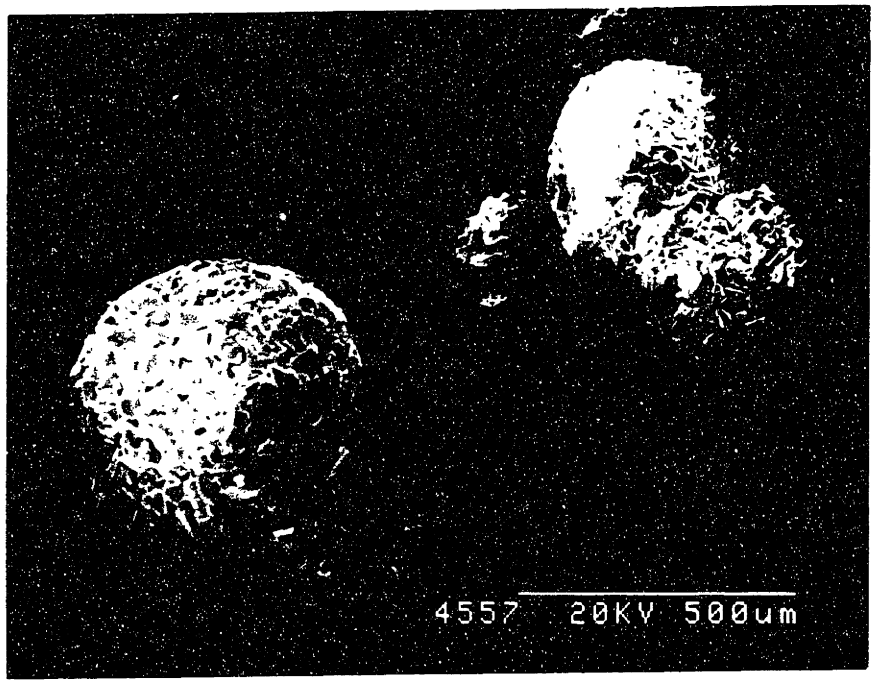

Figure 4.10 Micrograph showing several syringe drop primitives.

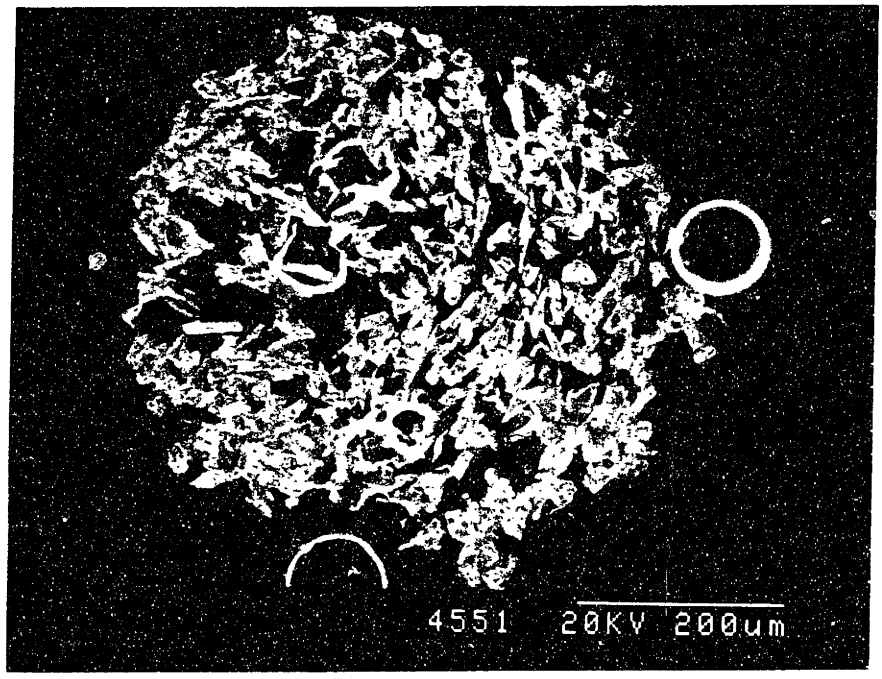

Figure 4.11 Scanning electron micrograph of a cross section through a syringe drop primitive.

Figure 4.12 Optical micrograph of the same syringe drop primitives using dual transmissive and reflective light sources.

Figure 4.13 High magnification of the surface of a 325 mesh primitive.

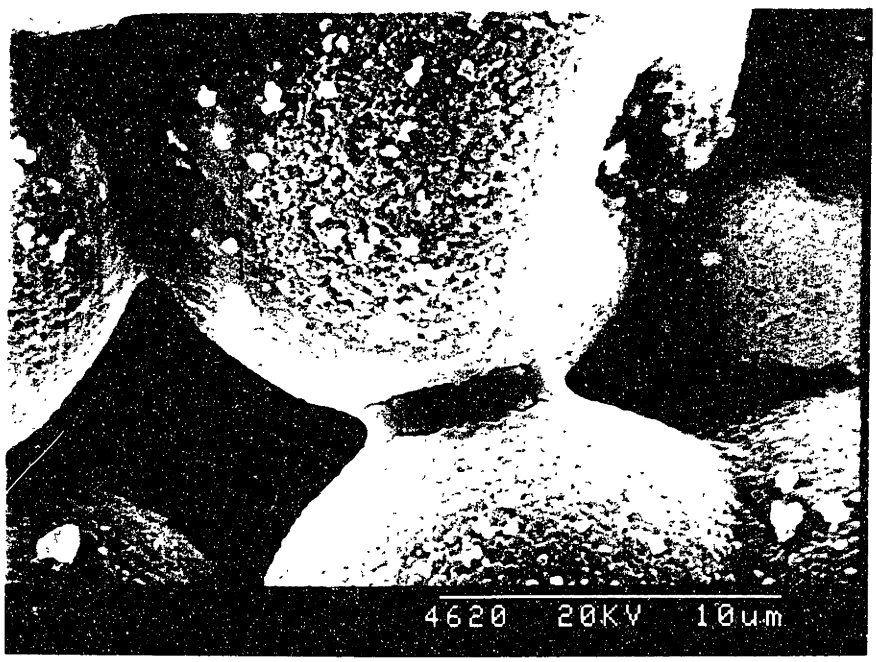

Figure 4.14 High magnification of the surface of a primitive made from in-house spray dried powder.

narrow and well defined. The silica does not coat the entire alumina particle and is only present close to the bridges. Again, cracking in the silica glass is visible.

SEM observations were also carried out on two kinds of 8 drop primitive segments; the Norton 30 μm alumina powder and the in-house spray dried powder. The 30 μm powder 8 drop segments are shaped like cylinders, sometimes bulging at the ends. They are about 500 μm in length and 200 μm in diameter. Figures 4.15 and 4.16 are micrographs of the 30 μm 8 drop segments.

The spray dried 8 drop segments also formed cylinders, but unlike the 30 μm segments they are curved. The curvature was observed both before and after the primitives were fired. The dimensions of the spray dried segments are very similar to those of the 30 μm segments. Figures 4.17 and 4.18 are micrographs of the 8 drop primitive segments made from the in-house spray dried powder.

Helium Pychnometer Measurements

A helium pychnometer was used to measure the skeletal density of many different kinds of primitives, as well as all the powders used in this study. In some cases, the amount of primitives recovered after printing was not large enough to allow accurate measurements using the helium pychnometer. The working fluid in this experiment is helium gas, therefore it can be assumed that all pores are infiltrated as long as no closed porosity exists, and the reported density represents the theoretical density for a particular mix of phases. The resulting data was used for composition analysis. Table 4.1 summarizes the results of the helium pychnometer experiments for the Norton 325 mesh powder, the Norton 30 μm powder, the in-house spray dried powder, the ICD spherical powder, the 30 μm single drop and 8 drop primitives, the spherical powder single drop primitives, and the spray dried powder 8 drop primitives. Density measurements for other kinds of primitives were obtained by mercury porosimetry.

Table 4.1 Helium Pychnometer Density Measurements.

Powders	**Density** (g/ml)	**Std. Dev.**
Norton 325 Mesh Alumina	3.97	0.02
Norton 30 μm Alumina	3.99	0.01
In-House Spray Dried Alumina	3.82	0.00
Showadenko 10 μm Spherical Alumina		
Primitives		
30 μm Single Drop Primitives	3.37	0.09
Spherical Powder Single Drop Primitives	3.38	0.02
30 μm 8 Drop Segment Primitives	3.59	0.01
Spray Dried Powder 8 Drop Segment Primitives	3.72	0.03

Figure 4.15 Micrograph of an 8 drop segment primitive made from Norton 30 μm alumina.

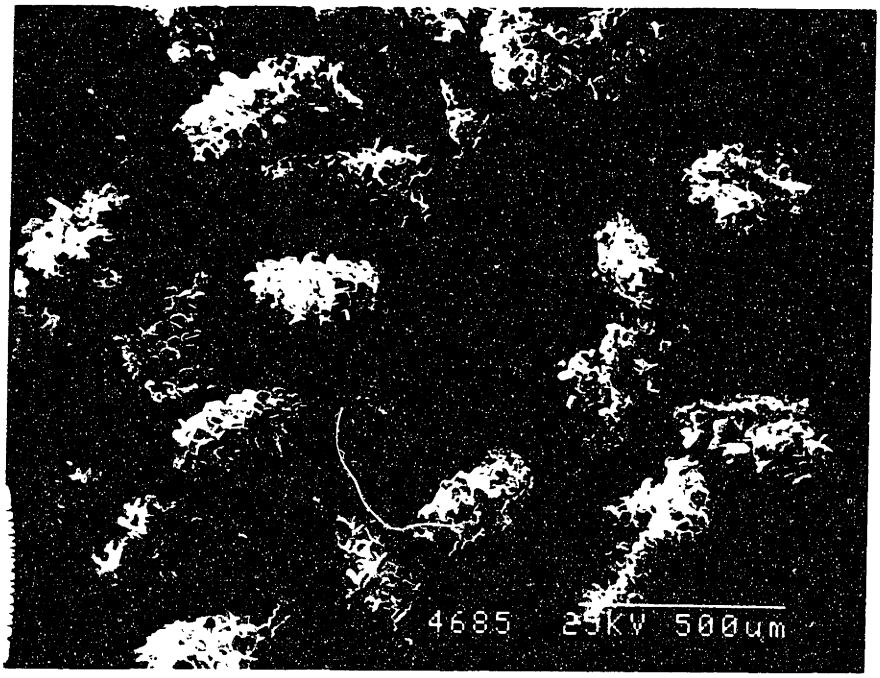

Figure 4.16 Micrograph of several 30 μm 8 drop primitives.

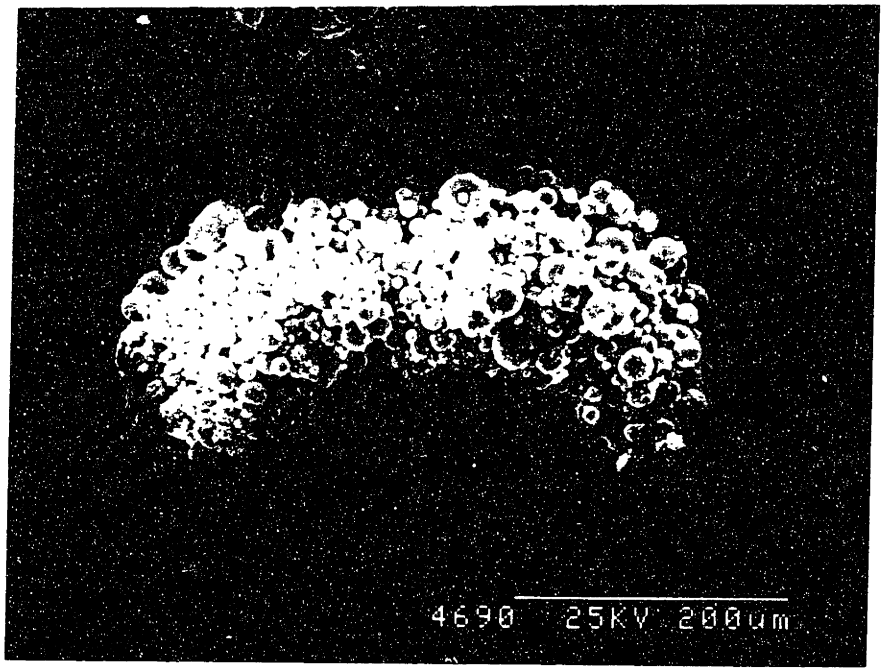

Figure 4.17 Micrograph of an 8 drop primitive segment made from the in-house spray dried alumina powder.

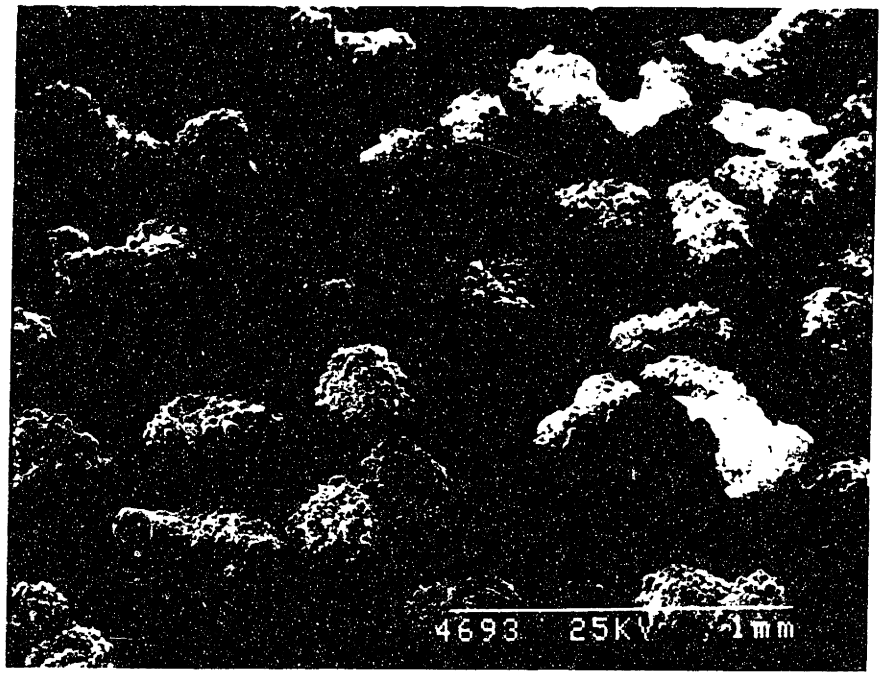

Figure 4.18 Micrograph of several spray dried 8 drop primitives.

Mercury Porosimetry Measurements

Mercury porosimetry was performed on all kinds of primitives and the four starting powders. The resulting porosity profiles were used to determine the bulk density of primitives and the extent of densification due to 3D Printing. The next few pages contain graphs of total intrusion volume versus pore diameter for each sample. Large pore sizes are infiltrated first due to the inverse relationship between infiltration pressure and pore size. Porosimetry data shows a general pattern of a short region of slow intrusion, due to packing of the sample, then another short region of very fast intrusion corresponding to interparticle filling. Finally, a long region of very slow or zero intrusion sets in as smallest pores are filled. The region of interparticle filling is usually large, and tends to obscure the actual pore distribution in the data for primitives. Corrections to the bulk density for primitive samples were made when necessary; these will be described in the Analysis section of this thesis. Figures 4.19 through 4.22 show the results of mercury porosimetry measurements for the four starting powders. Figures

4.23 through 4.28 are the porosity profile of each of the four kinds of single drop primitives, as well as the 30 μm 8 drop and spray dried 8 drop primitives. Table 4.2 gives the uncorrected bulk density obtained for each sample.

Table 4.2 Uncorrected Bulk Densities from Mercury Porosimetry.

Powders	**Bulk Density** (g/ml)
Norton 325 Mesh Alumina	1.60
Norton 30 μm Alumina	2.16
In-House Spray Dried Alumina	1.20
Showadenko 10 μm Spherical Alumina	2.23
Primitives	
325 Mesh Powder Single Drop Primitives	1.86
30 μm Powder Single Drop Primitives	1.21
Spray Dried Powder Single Drop Primitives	0.96
Spherical Powder Single Drop Primitives	3.09
30 μm Powder 8 Drop Segment Primitives	1.69
Spray Dried Powder 8 Drop Segment Primitives	1.25

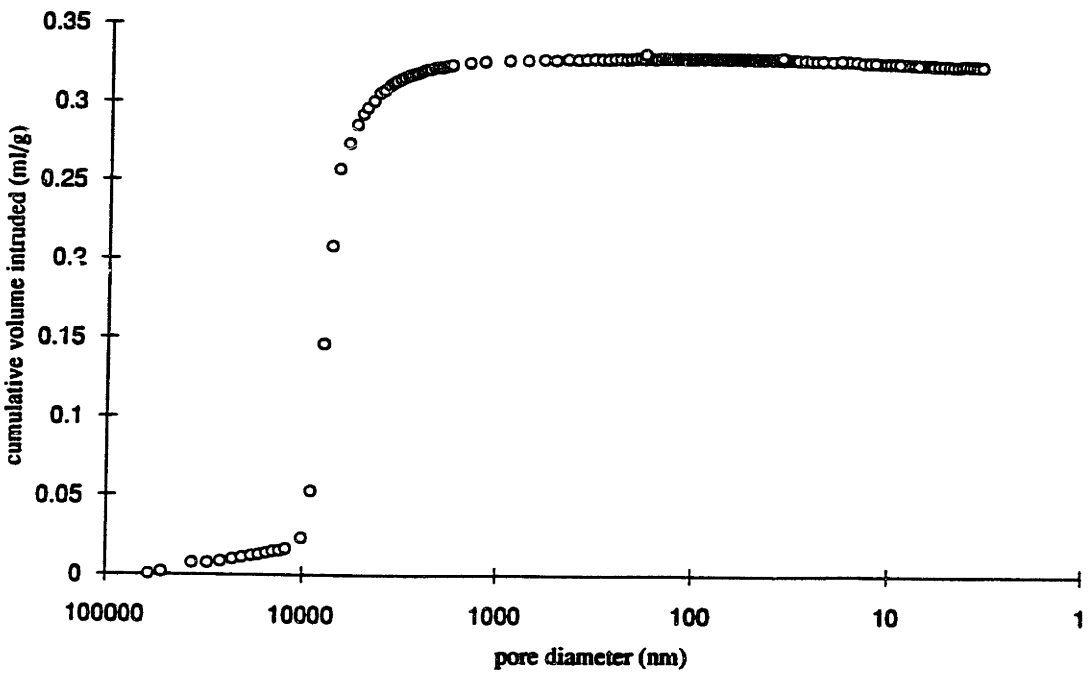

Figure 4.19 Mercury porosimetry data plot of pore size versus cumulative volume intruded for Norton 325 mesh alumina powder.

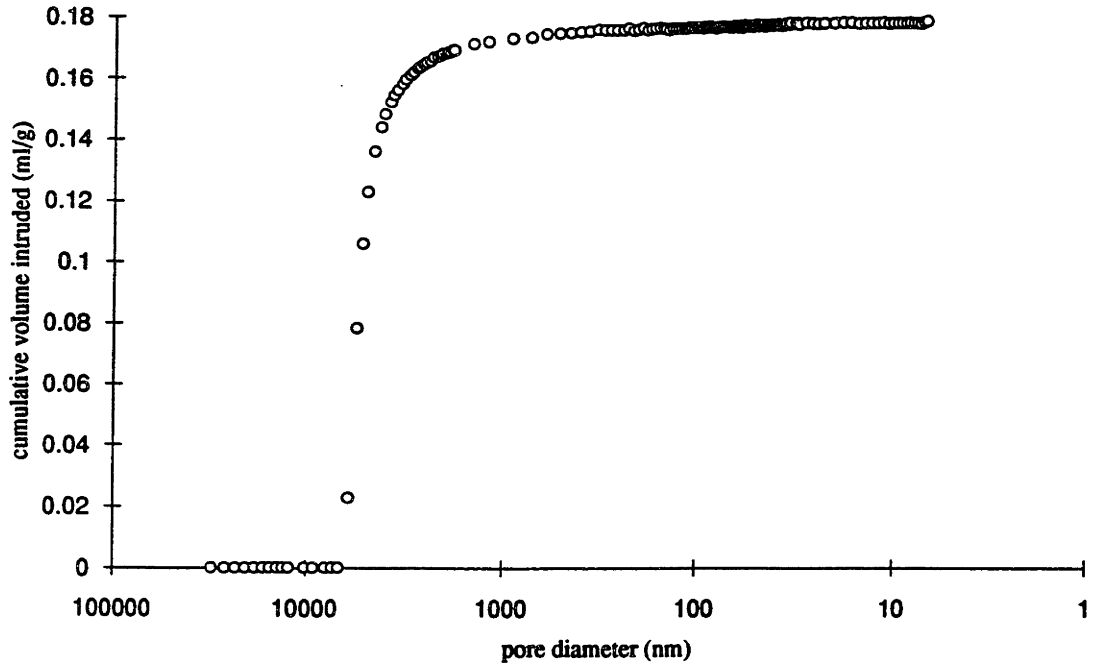

Figure 4.20 Mercury porosimetry data plot of pore size versus cumulative volume intruded for Norton 30 μm electronic grade alumina powder.

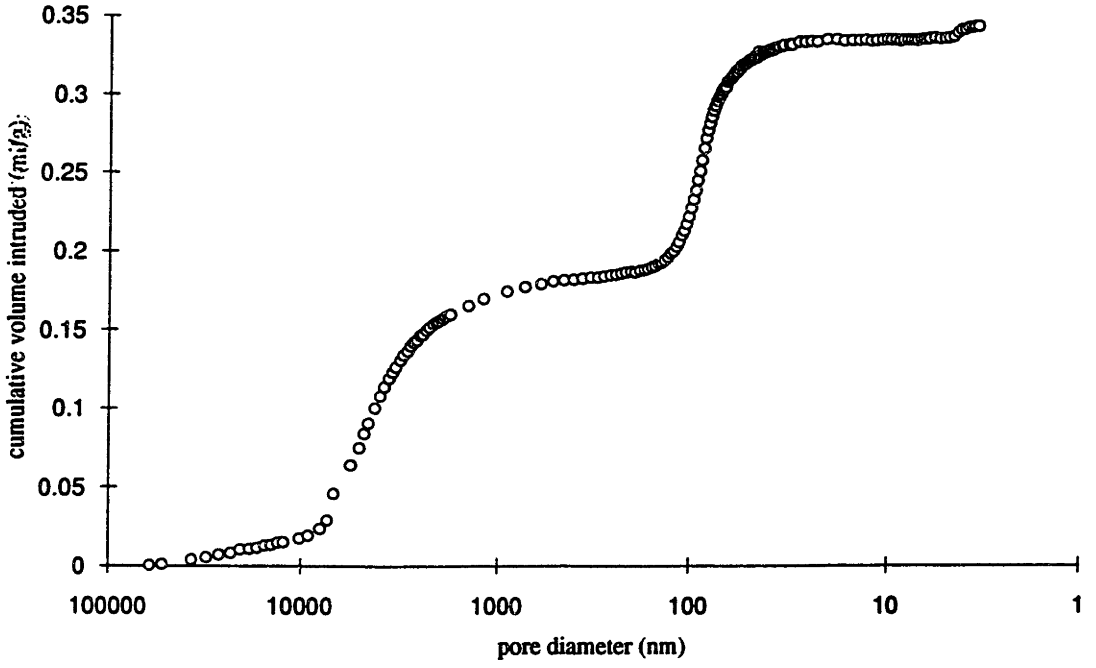

Figure 4.21 Mercury porosimetry data plot of pore size versus cumulative volume intruded for in-house spray dried alumina powder.

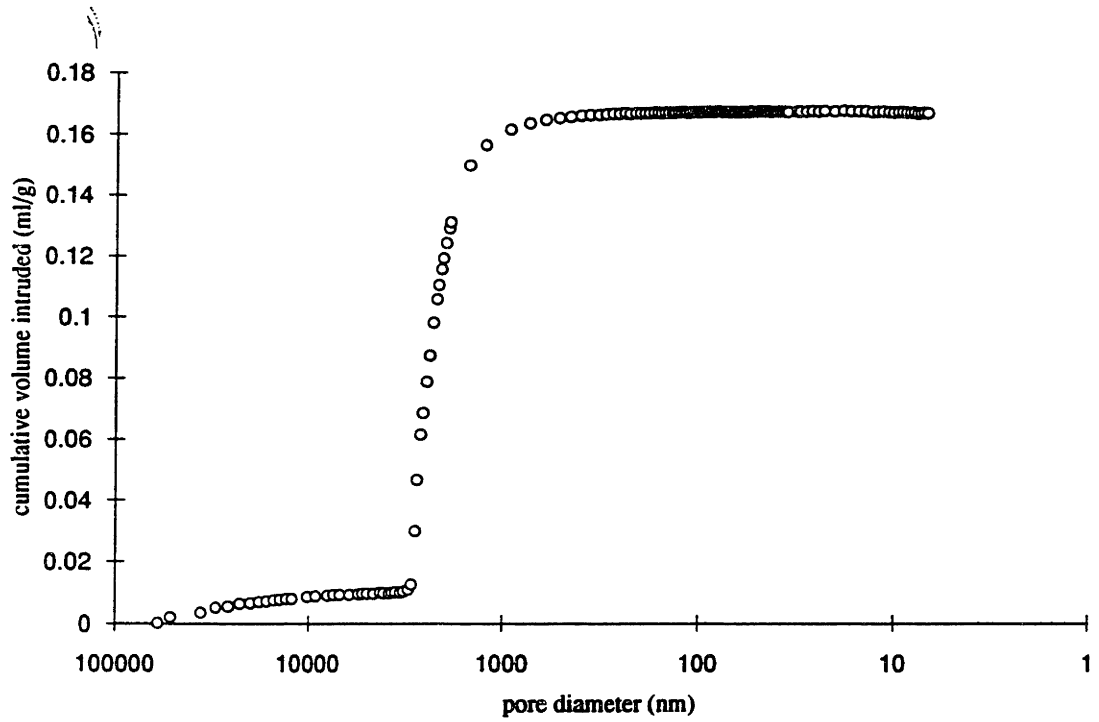

Figure 4.22 Mercury porosimetry data plot of pore size versus cumulative volume intruded for ICD 10 μm spherical alumina powder.

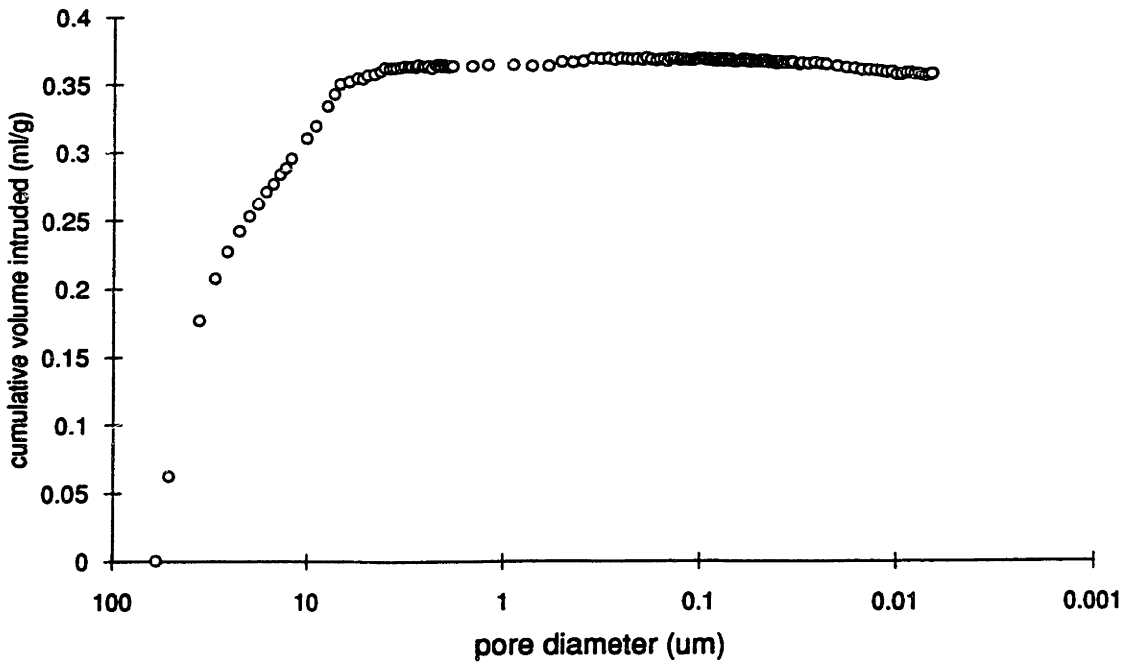

Figure 4.23 Mercury porosimetry data plot of pore size versus cumulative volume intruded for single drop primitives made with Norton 325 mesh powder.

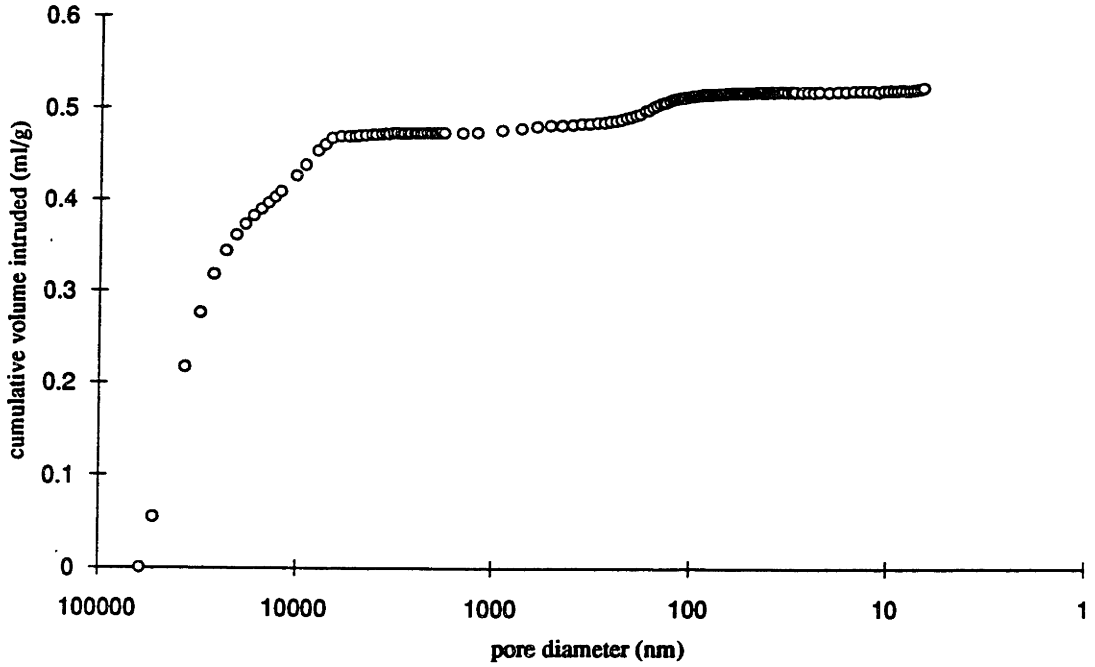

Figure 4.24 Mercury porosimetry data plot of pore size versus cumulative volume intruded for single drop primitives made with Norton 30 μm powder.

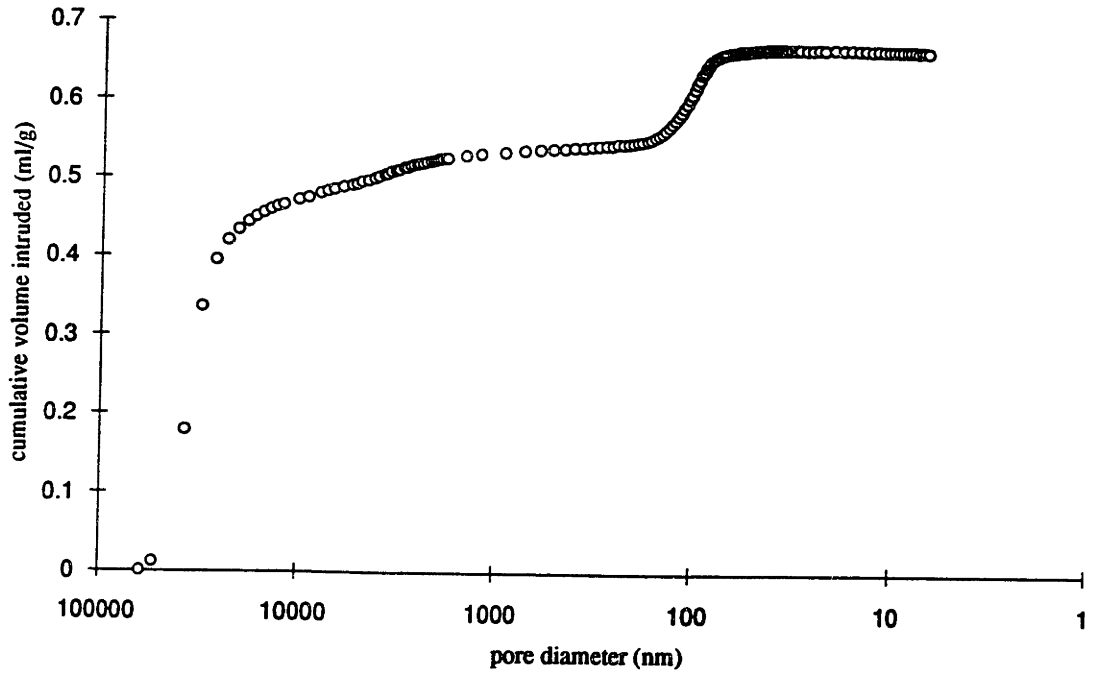

Figure 4.25 Mercury porosimetry data plot of pore size versus cumulative volume intruded for single drop primitives made with spray dried powder.

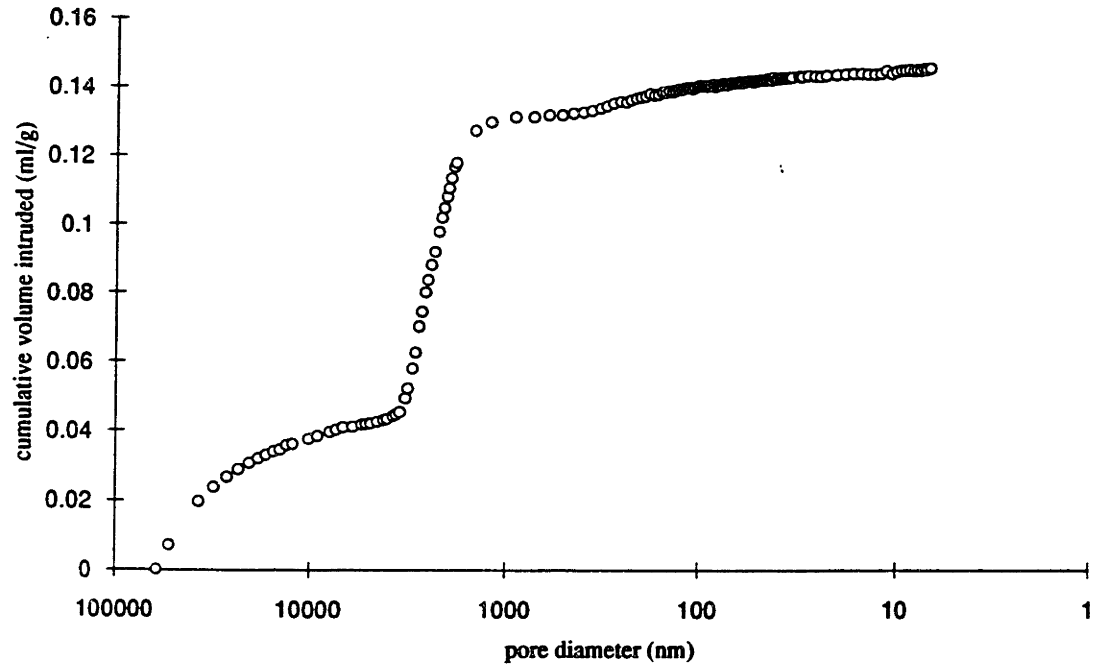

Figure 4.26 Mercury porosimetry data plot of pore size versus cumulative volume intruded for single drop primitives made with ICD spherical powder.

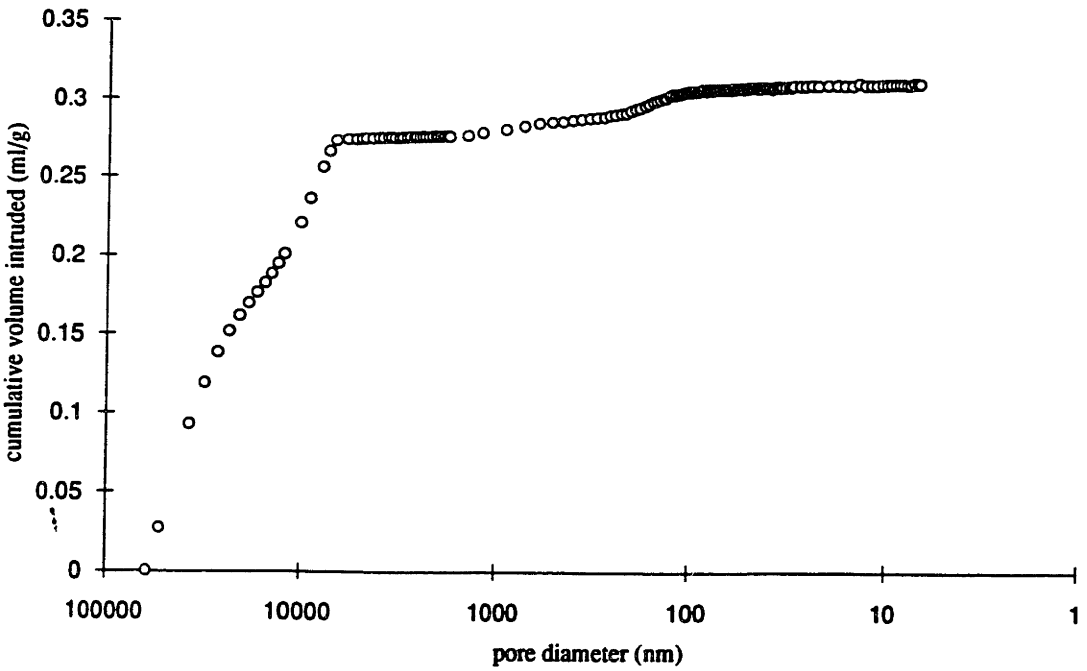

Figure 4.27 Mercury porosimetry data plot of pore size versus cumulative volume intruded for 8-drop primitives made with Norton 30 μm powder.

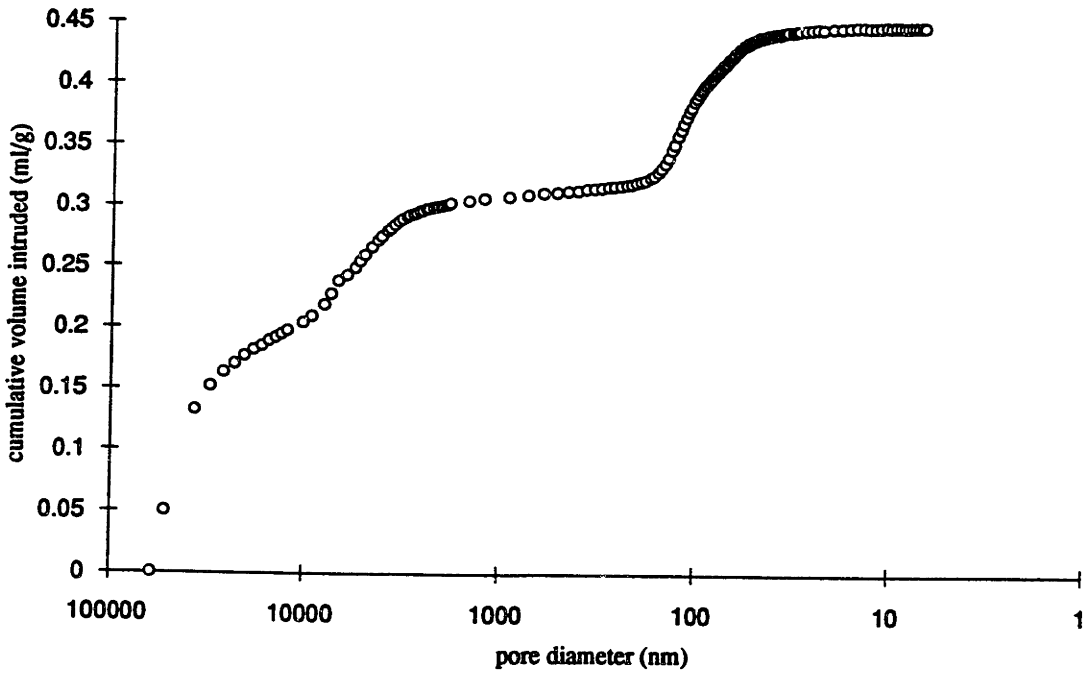

Figure 4.28 Mercury porosimetry data plot of pore size versus cumulative volume intruded for 8-drop primitives made with spray dried powder.

4.2 Lines

SEM Observations

Printed lines and pairs of adjacent lines were examined while still in the powder bed. Two important observations were made. First, lines were cylindrical in shape and were embedded in a U-shape trench in the powder bed. There was a visible gap of 50 to 100 μm between the edge of the printed line and the wall of the trench. Second, in cases where two lines had been printed adjacent to each other, only one line structure was visible. The diameter of the line structure varied with the line spacing that had been specified (see Figure 3.6). Line A, a single line, had a diameter of between 180 and 220 μm. Line set B, a pair of lines with center to center spacing of 89 μm, had a diameter of between 270 and 300 μm. Line set C, with a spacing of 178 μm, showed a diameter ranging from 350 to 380 μm. Figures 4.29 and 4.30 show two micrographs of a single

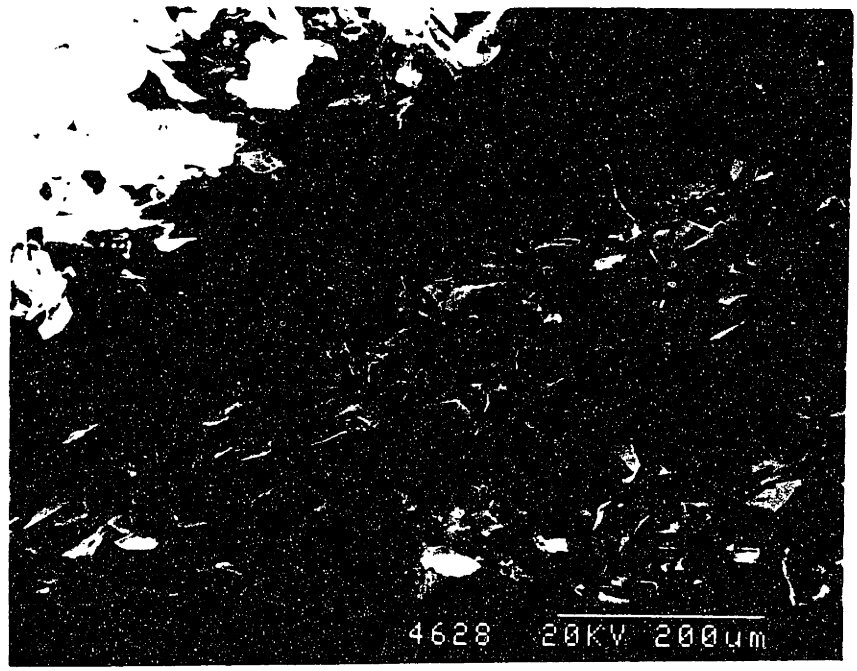

Figure 4.29 Scanning electron micrograph of a single printed line in the powder bed.

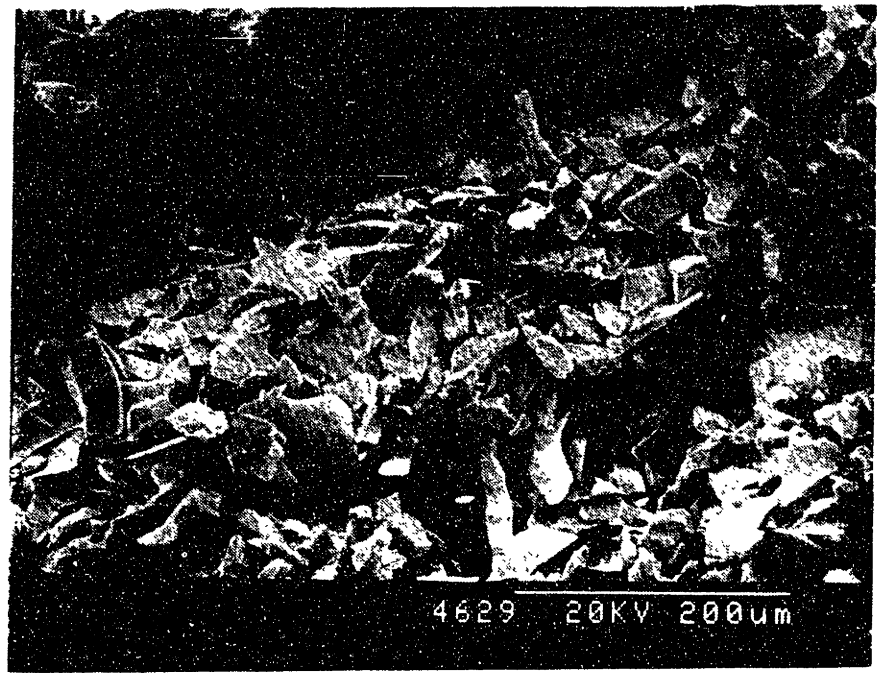

Figure 4.30 Scanning electron micrograph of a single printed line in the powder bed.

line printed into the powder bed. Micrographs of line pairs showed a similar structure with a larger diameter.

ESEM observations of line samples that had been placed in a humidity chamber after printing gave similar results to the standard SEM work. No evidence of any drying effects was visible in these experiments.

4.3 Walls

Wall Thickness Measurements

The thickness of each set of single line walls as described in Figure 3.7 was measured and plotted against binder content. Binder volume per unit line length, calculated from the binder flow rate and the printhead velocity for each wall, was used the measure of binder content. Faster printhead speeds resulted in a lower binder content. The results of the thickness measurements for 325 mesh powder with several different additives are plotted in Figure 4.31. The layer thickness for the shown data was 250 μm.

Single line walls were also examined by SEM and optical microscopy. Cross sections of a wall made with 2% polyacrylic acid, 2% citric acid, and no additive are shown in Figures 4.32 to 4.34. The fast printing axis is perpendicular to the plane of the photograph in these pictures.

Multiple Line Walls

Multiple line walls were examined by SEM. Cross sections of walls 3B and 4B (as described in Figure 3.9) are shown in Figures 4.35 and 4.36. These walls were made using 325 mesh powder. Two important features are visible in these photographs. First, individual layers and lines within layers are clearly visible. The lines are seen to have a circular cross section of densely packed powder, with little powder present between lines. Second, pairs of adjacent lines appear to have joined together along their long axis. This

has created a defect in between pairs of joined lines. These features were found in all samples of multiple line walls.

Multiple line walls built using the in-house spray dried powder and the ICD spherical powder were also examined. Texturing due to individual lines was visible in these samples also. The spray dried walls exhibited the same kind of curvature seen in the 8-drop spray dried primitives. Producing a wall from spray dried powder that was more than a few layers thick proved to be extremely difficult because the ends of the wall would curl up above the plane of the powder bed, preventing the spreading of a new layer without destroying the part in progress. This problem was solved to some extent by spraying water on the powder bed from an aspirator bottle until it was pasty before spreading a new layer. This technique repressed the curling action enough to allow new layers to be spread without demolishing the part. Figure 4.37 is a cross section of a 5 line thick spherical powder wall. Figure 4.38 shows a cross section of a 15 line thick wall made using spray dried powder.

Mercury porosimetry measurements of pore size distribution and density were also carried out on wall samples. These experiments were done for walls made from 325 mesh powder, in house spray dried powder, and ICD spherical powder. Graphs of pore size versus cumulative volume of mercury intruded are shown in Figures 4.39 - 4.41. Wall samples typically show little extraneous intrusion at low pressures because there are no large voids to be filled, in contrast to primitive samples in which the voids between each primitive must be filled before meaningful results can be obtained. Wall samples do show a small tail at the largest pore sizes, however. This is likely due to sample rearrangement during filling and is easily corrected for.

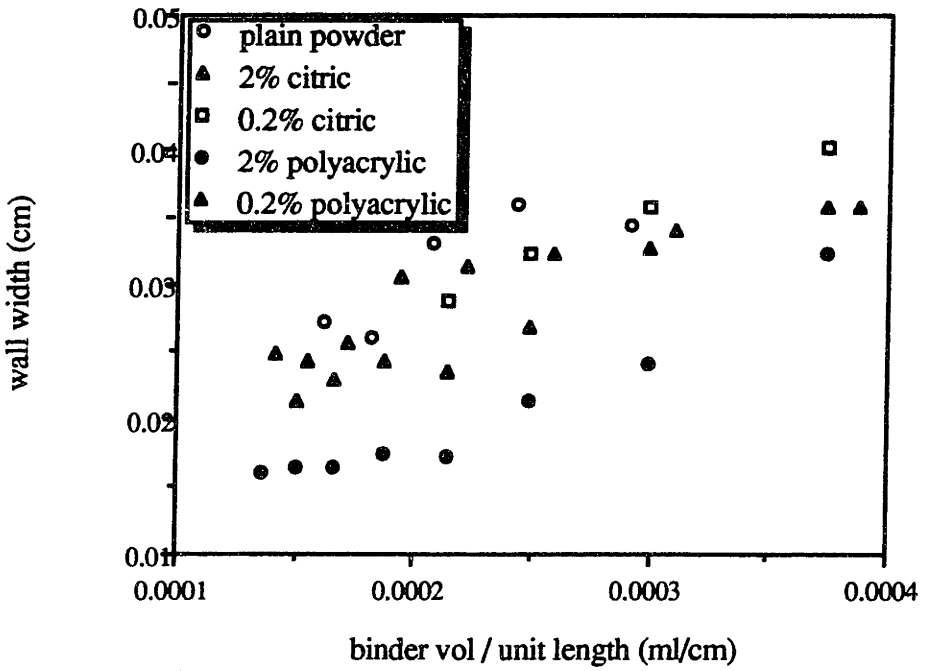

Figure 4.31 Wall width versus binder content for 325 mesh powder walls with a 250 μm layer thickness. Results are shown for four different additives and plain powder.

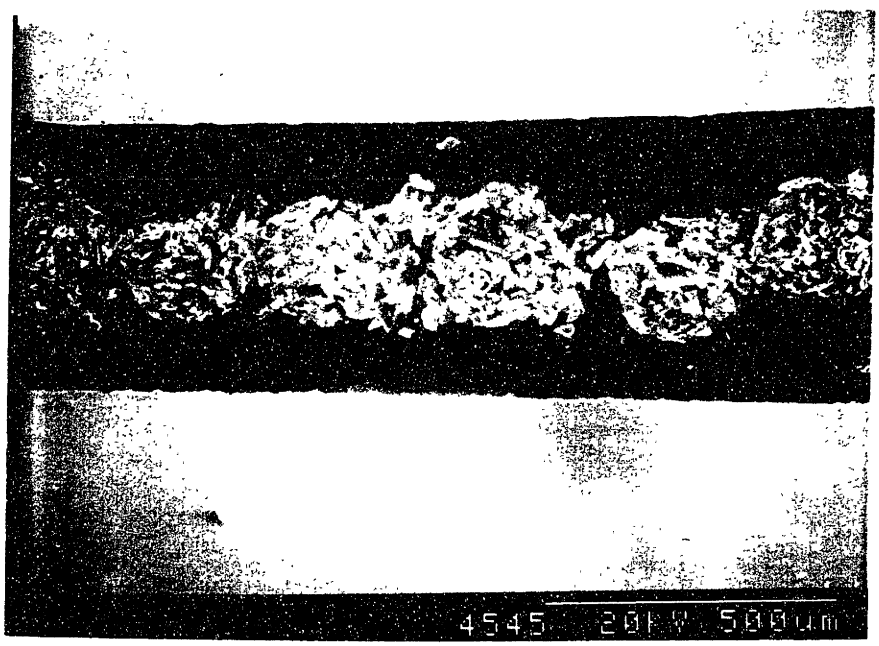

Figure 4.32 Cross section of a single line wall made with 2% polyacrylic acid additive.

Figure 4.33 Cross section of a single line wall made with 2% citric acid additive.

Figure 4.34 Cross section of a single line wall made with no additive.

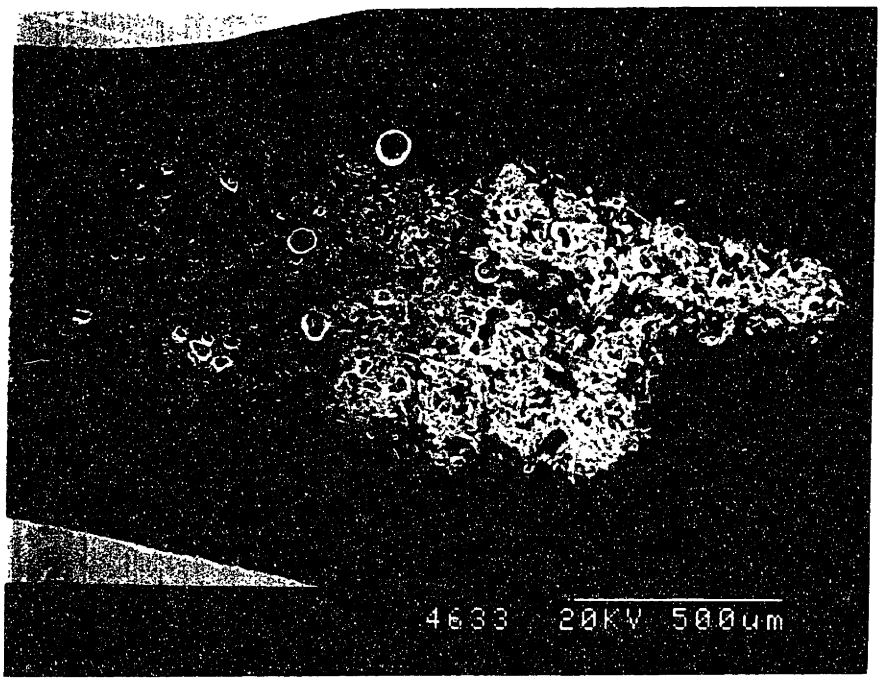

Figure 4.35 Cross section of 3 line wall (sample 3B).

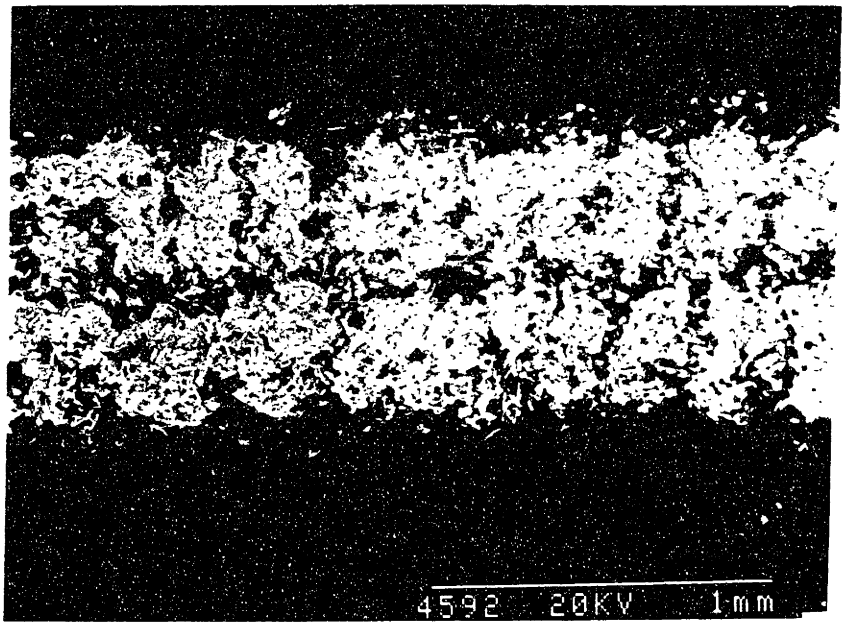

Figure 4.36 Cross section of 4 line wall (sample 4B).

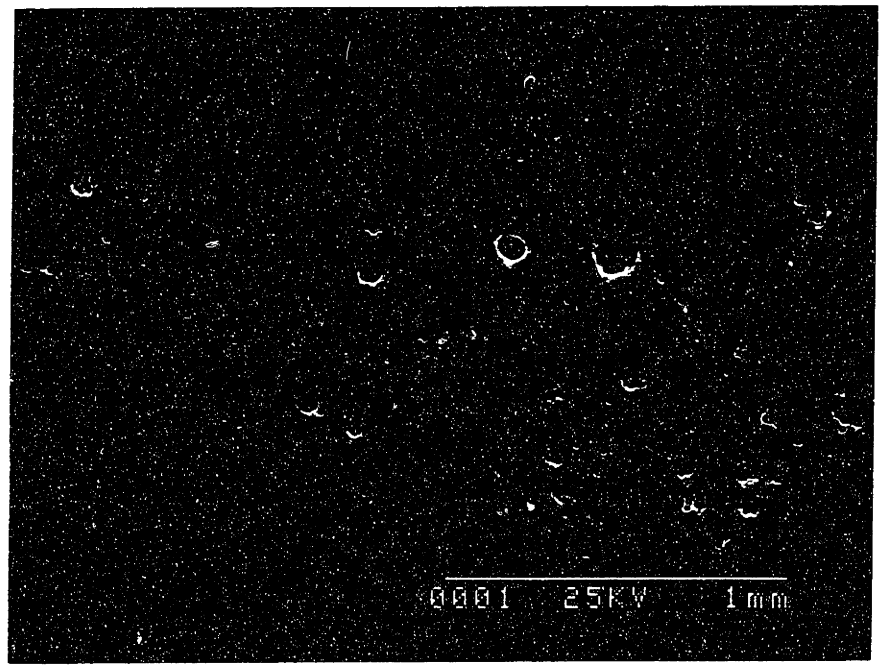

Figure 4.37 Cross section of a 5 line spherical powder wall.

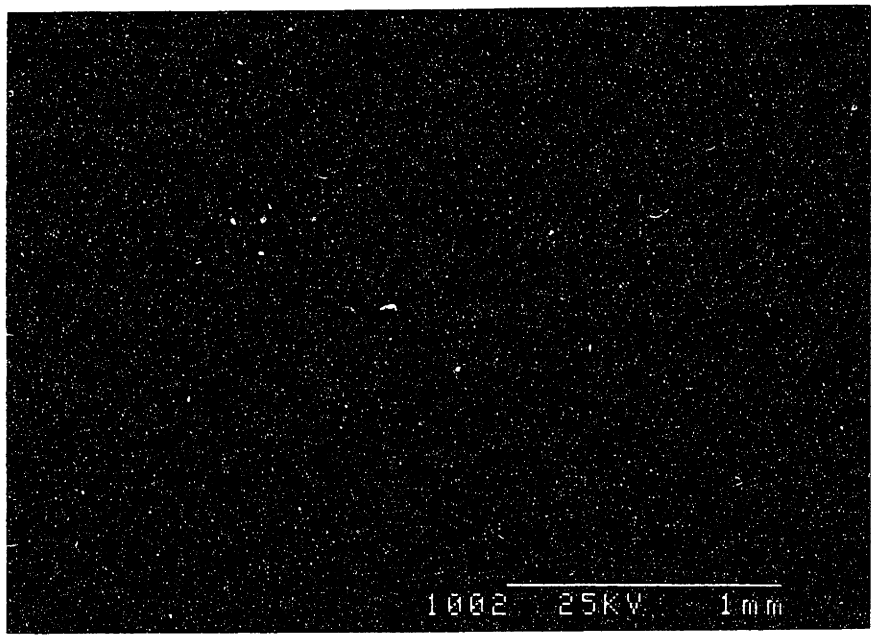

Figure 4.38 Cross section of a 15 line thick spray dried powder wall.

5. ANALYSIS

5.1 Primitive Porosimetry Analysis

Skeletal density data for individual primitives can be used to determine the relative amounts of alumina and silica each contains. Bulk density measurements from mercury porosimetry can be used to find the average density of primitive structures, including the ratio of solids (sum of alumina and silica) to voids. These results in combination give the amount that the alumina powder packing increased, as well as the volume fractions of alumina, silica and voids in each primitive sample. Helium pychnometry measurements provide accurate skeletal density figures in most cases. Mercury porosimetry calculates the bulk sample volume by subtracting the volume of mercury forced into the sample chamber at low pressure from the volume of the sample chamber. The filling pressures are not high enough to force mercury in between individual primitives, thus bulk densities from mercury porosimetry are subject to error due to extraneous mercury intrusion during interprimitive filling of the sample chamber and require correction.

Volume Corrections for Hg Porosimetry

Three strategies were considered for estimating the intrusion volume due to interprimitive filling in porosimetry samples. The first was to model the pores between primitives as octahedral voids in a close packed structure. Assuming solid, uniformly sized spheres, these pores can be shown to have a diameter of 0.83r, where r is the primitive radius. Taking the primitive diameter as 200 μm, the modeled pore size is 83 μm, which is larger than the pore size infiltrated at the initial filling pressure. This predicts that all interprimitive filling takes place immediately, so no volume correction is required and the uncorrected bulk densities presented in Table 4.2 are correct. Clearly, this model does not sufficiently describe the filling of primitive samples as evidenced by the unreasonably low bulk densities it predicts and it lack of explanation for the initial tail in the filling profiles.

A second strategy was to assume all filling of pores larger than the largest observed pore size in primitive samples was interprimitive filling, and subtract this volume from the reported sample volume. Primitives were viewed by SEM to find the largest pore sizes typically observed. Only fully developed pores into the primitive were used for these estimates; surface indentations, possibly due to a missing particle, were not included. Depending on the type of sample, the largest observed pore sizes were between 3 μm and 15 μm.

The third method was to compare the porosimetry data for primitive samples with the data for the powders they were made from. It was assumed that there were no pores in the primitives larger than the largest pores found in the loose powder. This is a

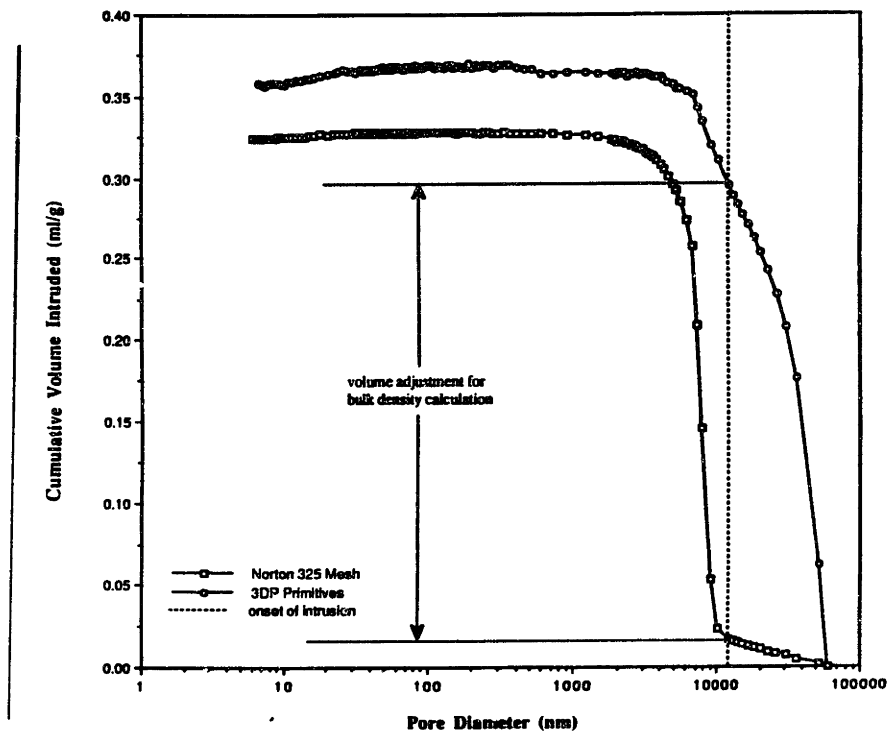

Figure 5.1 Comparison of primitive and powder porosimetry results to predict the necessary volume correction due to interprimitive filling.

reasonable assumption because primitives contain silica glass between the particles, effectively reducing the interparticle pore size. The intrusion volumes for the primitive and powder samples were compared at the largest pore size found in the powder, and the

difference between the intrusion volumes was taken to be the interprimitive pore volume. This volume was then subtracted from the reported sample volume, and the bulk density was recalculated using the corrected sample volume. This comparison process is graphically illustrated in Figure 5.1. The powder comparison method and the largest observable pore size method generally showed good agreement, but the comparison method was chosen as the standard since it relied on hard data rather than random observations.

Primitive Composition

Corrected bulk densities were used to calculate densification of the powder bed during printing for each type of sample. Skeletal densities were used to calculate the volume fractions of silica and alumina for each type of primitive, using the known densities of the alumina powder and the silica glass. The results of these calculations for the 325 mesh single drop primitives, the Norton 30 μm single drop primitives, the in-house spray dried single drop primitives, the ICD spherical single drop primitives, the Norton 30 μm 8 drop primitives, and the spray dried 8 drop primitives are presented in Tables 5.1 through 5.6 respectively. Each table contains a description of the type of primitive and powder, a list of the constants used in the calculations, a summary of the porosimetry data, and the value for the volume correction due to interprimitive filling. The resulting bulk density, the skeletal density from helium pychnometer measurements, the compositional analysis, and the extent of densification of the loose powder calculated from primitive bulk density, are also presented, along with a chart of the volume fractions of alumina, silica, and voids that make up the primitive. Figure 5.2 summarizes the composition results for primitives.

Table 5.1 Composition and Densification for 325 mesh Single Drop Primitives

PRIMITIVE DENSITY CALCULATIONS

TYPE:	**Norton 325 Mesh Single Drop Primitives**		
POWDER:	Norton 325 Mesh Alumina		
POWDER DENSITY:	3.97	g/ml	
PACKING DENSITY:	1.39	g/ml	
SILICA DENSITY:	2.19	g/ml	

POROSIMETRY DATA:

Penetrometer #:	14-0259		
Penetrometer volume:	3.2134	ml	
Penetrometer weight:	69.422	g	
Sample weight:	0.250	g	
Pen + Sample + Hg:	110.907	g	
Maximum intrusion volume:	0.369	ml/g	
Volume correction:	0.0698	ml	(predicted by comparison to powder porosimetry results)
Adjusted Bulk Density:	2.58	g/ml	(calculated from porosimetry data)
Skeletal Density:	3.37	g/ml	(measured by helium pychnometer)

COMPOSITION:

Solid Volume Fraction:	0.768
Voids Volume Fraction:	0.232
Solid Composition by volume:	
Alumina:	0.661
Silica:	0.339
Overall Composition:	
Alumina	**0.507**
Silica	**0.261**
Voids	**0.232**

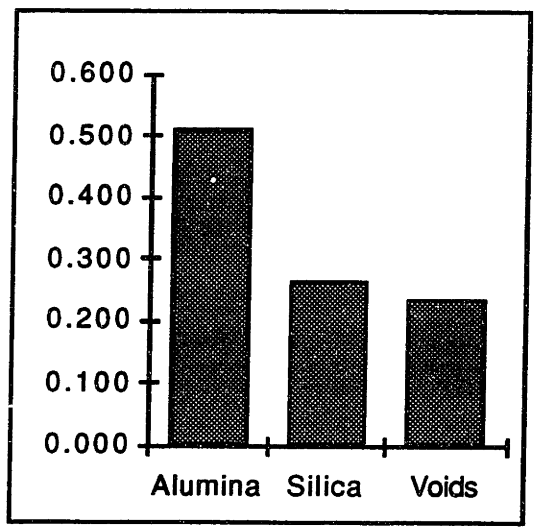

DENSIFICATION:

Overall Densification from	**1.39**	to	**2.58**	**86.0%**
Alumina Packing increase from	**1.39**	to	**1.71**	**22.9%**

Table 5.2 Composition and Densification for Norton 30 μm Single Drop Primitives

PRIMITIVE DENSITY CALCULATIONS

TYPE:	**Norton 30 μm Single Drop Primitives**		
POWDER:	Norton 30 μm Alumina		
POWDER DENSITY:	3.99	g/ml	
PACKING DENSITY:	1.39	g/ml	
SILICA DENSITY:	2.19	g/ml	

POROSIMETRY DATA:

Penetrometer #:	14-0264		
Penetrometer volume:	3.3056	ml	
Penetrometer weight:	68.078	g	
Sample weight:	0.492	g	
Pen + Sample + Hg:	108.282	g	
Maximum intrusion volume:	0.5202	ml/g	
Volume correction:	0.1891	ml	(predicted by comparison to powder porosimetry results)
Adjusted Bulk Density:	2.70	g/ml	(calculated from porosimetry data)
Skeletal Density:	3.37	g/ml	(measured by helium pychnometer)

COMPOSITION:

Solid Volume Fraction:	0.802
Voids Volume Fraction:	0.198
Solid Composition by volume:	
Alumina:	0.653
Silica:	0.347
Overall Composition:	
Alumina	**0.524**
Silica	**0.278**
Voids	**0.198**

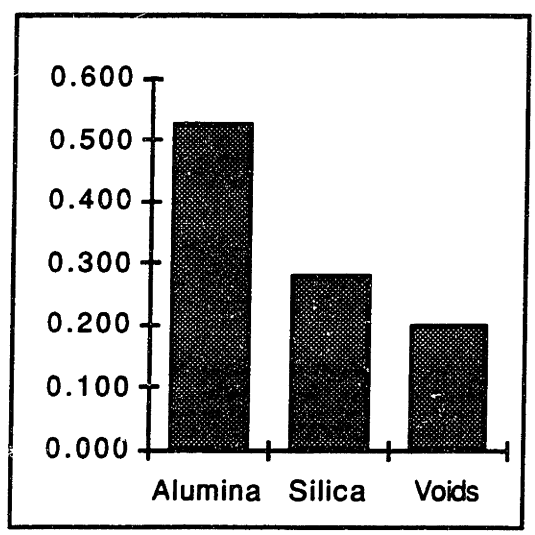

DENSIFICATION:

Overall Densification from	**1.91**	to	**2.70**	**41.4%**
Alumina Packing increase from	**1.91**	to	**2.09**	**9.5%**

Table 5.3 Composition and Densification for Spray Dried Single Drop Primitives

PRIMITIVE DENSITY CALCULATIONS

TYPE:	**Spray Dried Single Drop Primitives**	
POWDER:	In-House Spray Dried Alumina	
POWDER DENSITY:	3.82	g/ml
PACKING DENSITY:	1.10	g/ml
SILICA DENSITY:	2.19	g/ml

POROSIMETRY DATA:

Penetrometer #:	14-0259		
Penetrometer volume:	3.2134	ml	
Penetrometer weight:	68.890	g	
Sample weight:	0.540	g	
Pen + Sample + Hg:	106.041	g	
Maximum intrusion volume:	0.6663	ml/g	
Volume correction:	0.2498	ml	(predicted by comparison to powder porosimetry results)
Adjusted Bulk Density:	2.09	g/ml	(calculated from porosimetry data)
Skeletal Density:	3.64	g/ml	(measured by helium pychnometer)

COMPOSITION:

Solid Volume Fraction:	0.574
Voids Volume Fraction:	0.426
Solid Composition by volume:	
Alumina:	0.889
Silica:	0.111
Overall Composition:	
Alumina	**0.511**
Silica	**0.064**
Voids	**0.426**

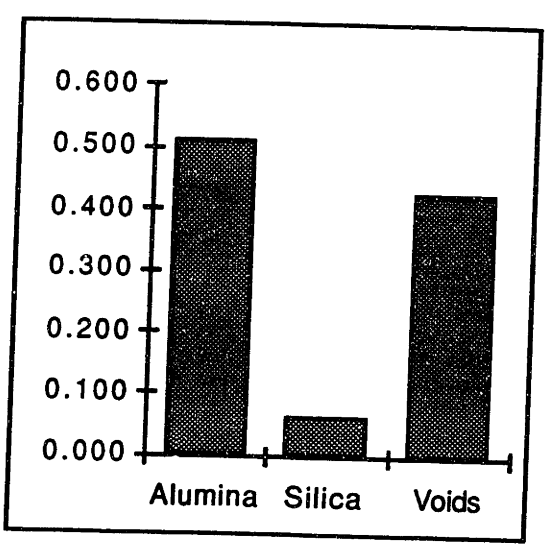

DENSIFICATION:

Overall Densification from	**1.10**	to	**2.09**	**90.0%**
Alumina Packing increase from	**1.10**	to	**1.95**	**77.3%**

Table 5.4 Composition and Densification for ICD Spherical Single Drop Primitives

PRIMITIVE DENSITY CALCULATIONS

TYPE:	**Spherical Powder Single Drop Primitives**		
POWDER:	ICD 10 μm Spherical Alumina		
POWDER DENSITY:	3.97	g/ml	
PACKING DENSITY:	1.90	g/ml	
SILICA DENSITY:	2.19	g/ml	

POROSIMETRY DATA:

Penetrometer #:	14-0264		
Penetrometer volume:	3.3056	ml	
Penetrometer weight:	68.306	g	
Sample weight:	0.859	g	
Pen + Sample + Hg:	108.785	g	
Maximum intrusion volume:	0.1429	ml/g	
Volume correction:	0.0290	ml	(predicted by comparison to powder porosimetry results)
Adjusted Bulk Density:	2.46	g/ml	(calculated from porosimetry data)
Skeletal Density:	3.53	g/ml	(measured by helium pychnometer)

COMPOSITION:

Solid Volume Fraction:	0.697
Voids Volume Fraction:	0.303
Solid Composition by volume:	
Alumina:	0.753
Silica:	0.247
Overall Composition:	
Alumina	**0.525**
Silica	**0.172**
Voids	**0.303**

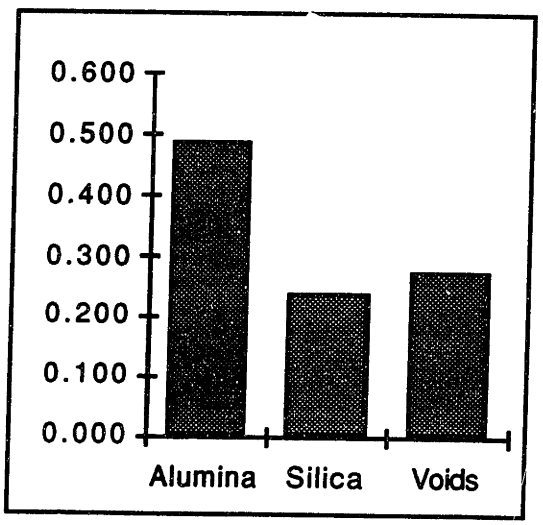

DENSIFICATION:

Overall Densification from	**1.90**	to	**2.46**	**29.5%**
Alumina Packing increase from	**1.90**	to	**2.08**	**9.7%**

Table 5.5 Composition and Densification for Norton 30 μm 8 Drop Primitives

PRIMITIVE DENSITY CALCULATIONS

TYPE:	**Norton 30 μm 8-Drop Primitives**		
POWDER:	Norton 30 μm Alumina		
POWDER DENSITY:	3.99	g/ml	
PACKING DENSITY:	1.91	g/ml	
SILICA DENSITY:	2.19	g/ml	

POROSIMETRY DATA:

Penetrometer #:	14-0259		
Penetrometer volume:	3.2134	ml	
Penetrometer weight:	68.344	g	
Sample weight:	0.610	g	
Pen + Sample + Hg:	107.549	g	
Maximum intrusion volume:	0.3085	ml/g	
Volume correction:	0.1103	ml	(predicted by comparison to powder porosimetry results)
Adjusted Bulk Density:	2.43	g/ml	(calculated from porosimetry data)
Skeletal Density:	3.59	g/ml	(measured by helium pychnometer)

COMPOSITION:

Solid Volume Fraction:	0.676
Voids Volume Fraction:	0.324
Solid Composition by volume:	
Alumina:	0.778
Silica:	0.222
Overall Composition:	
Alumina	**0.526**
Silica	**0.150**
Voids	**0.324**

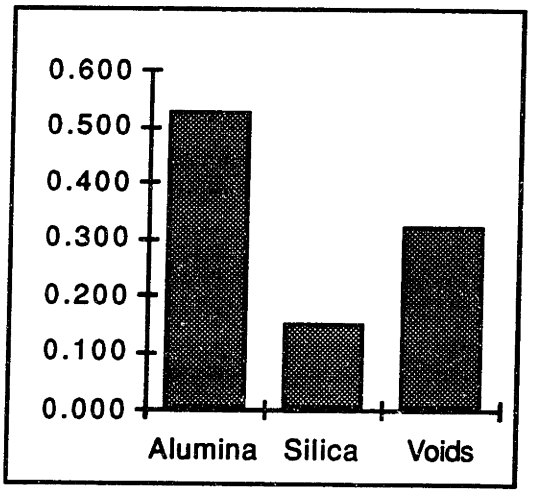

DENSIFICATION:

Overall Densification from	**1.91**	to	**2.43**	**74.6%**
Alumina Packing increase from	**1.91**	to	**2.10**	**9.9%**

Table 5.6 Composition and Densification for Spray Dried 8 Drop Primitives

PRIMITIVE DENSITY CALCULATIONS

TYPE:	**Spray Dried 8-Drop Primitives**		
POWDER:	In-house Spray Dried Alumina		
POWDER DENSITY:	3.82	g/ml	
PACKING DENSITY:	1.10	g/ml	
SILICA DENSITY:	2.19	g/ml	

POROSIMETRY DATA:

Penetrometer #:	14-0264		
Penetrometer volume:	3.3056	ml	
Penetrometer weight:	67.494	g	
Sample weight:	0.783	g	
Pen + Sample + Hg:	105.336	g	
Maximum intrusion volume:	0.4472	ml/g	
Volume correction:	0.1711	ml	(predicted by comparison to powder porosimetry results)
Adjusted Bulk Density:	1.98	g/ml	(calculated from porosimetry data)
Skeletal Density:	3.72	g/ml	(measured by helium pychnometer)

COMPOSITION:

Solid Volume Fraction:	0.531
Voids Volume Fraction:	0.469
Solid Composition by volume:	
Alumina:	0.939
Silica:	0.061
Overall Composition:	
Alumina	**0.499**
Silica	**0.033**
Voids	**0.469**

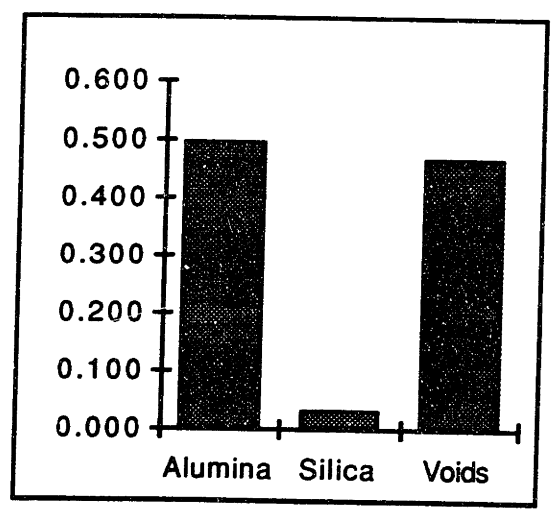

DENSIFICATION:

Overall Densification from	**1.10**	to	**1.98**	**80.0%**
Alumina Packing increase from	**1.10**	to	**1.10**	**73.3%**

Primitive Densification

Primitives show a denser alumina packing than is found in the loose powder bed, as illustrated in Figure 5.3. The extent of densification varies depending on the powder that the primitive was made from. Figure 5.4 summarizes the measured density results

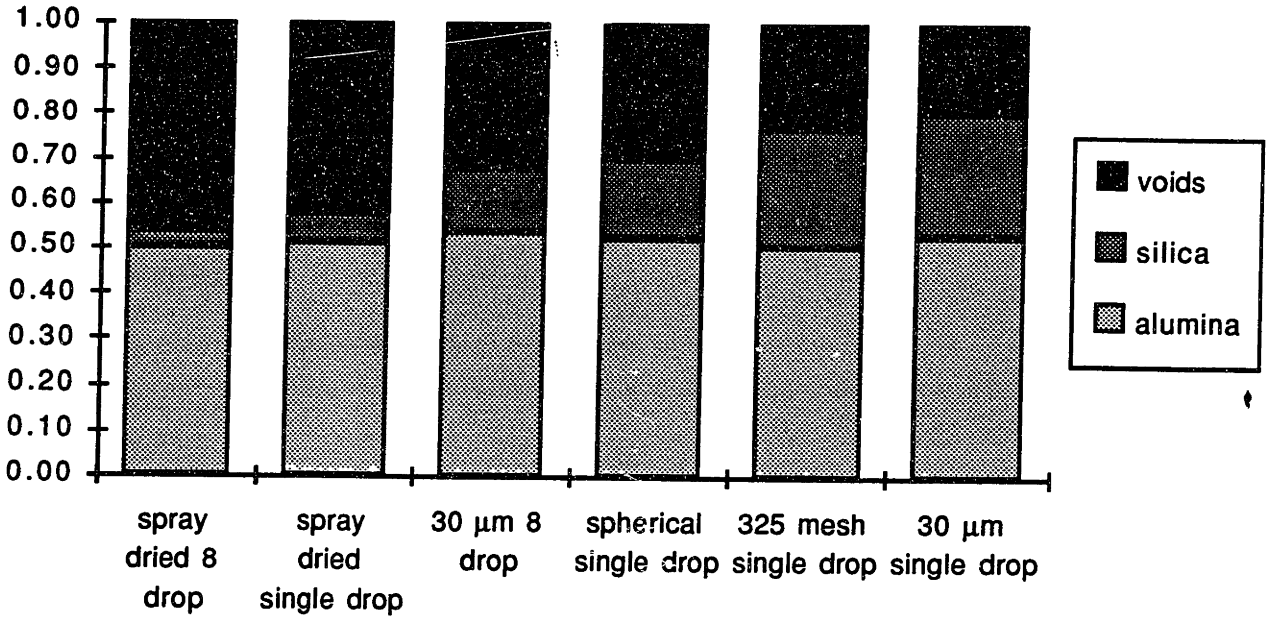

Figure 5.2 Summary of primitive compositions by volume fraction.

for each kind of primitive. An important result of this graph is the trend that as bulk density increase, skeletal density decreases. Also, primitives made from spherical shaped powders show lower bulk density and higher skeletal density than those made from faceted powders.

These results can be explained by assuming that surface tension of the binder is responsible for causing densification of the primitives. As the binder droplet penetrates the powder bed, liquid coats the particles. Capillary pressure draws binder selectively into the necks between particles. The liquid attempts to minimize its surface energy by reducing its surface to volume ratio and minimizing the area of liquid/vapor interfaces.

The result is a densification of the powder particles. As the liquid dries, particles may be pulled together more tightly causing further densification. The influence of surface tension forces will be greater in powder beds more susceptible to rearrangement, such as those with low initial packing densities or spherical particles.

High magnification micrographs of primitives show differences in the silica bridging between particles for the different samples. Micrographs of the 325 mesh and 30 μm primitives show large silica bridges between particles, covering the entire surface area of the alumina. As a result, pore in the primitives are largely filled with silica glass. The has the effect of lowering the skeletal density of the primitive because of the large volume fraction of silica, while at the same time increasing the bulk density by lowering the void volume. This type of wide area silica bridge is not the most effective at pulling particles together, however, so the alumina packing increase for faceted powders tends to be low.

Micrographs of the bridges between spherical particle show small amounts of silica only present in the necks between particles. The small amount of silica required to bond particles leaves the interparticle pores largely open, thus reducing the bulk density. Since less silica is present for each pair of alumina particles, however, the skeletal density of these primitives is high. Also, the small cylindrical bridges between particles provides a higher capillary pressure, tending to increase the alumina particle packing in these powders more than in the faceted powders. The porous spray dried powder is found to have a lower bulk density than the solid ICD spherical powder, as expected. The surface tension mechanism can also be used to explain the spherical shape of primitives. The binder droplet pulls alumina particles in and causes them to densify while minimizing its surface energy by assuming a spherical shape. Thus, the shape of the binder droplet governs the shape of the primitive.

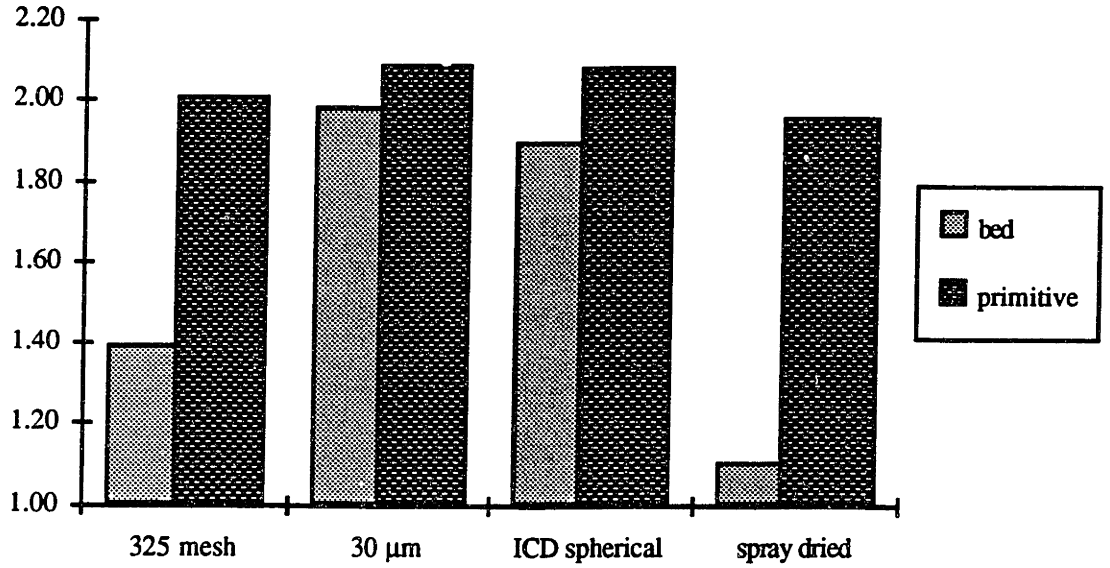

Figure 5.3 Alumina packing (ml/g) in primitives vs. in the powder bed.

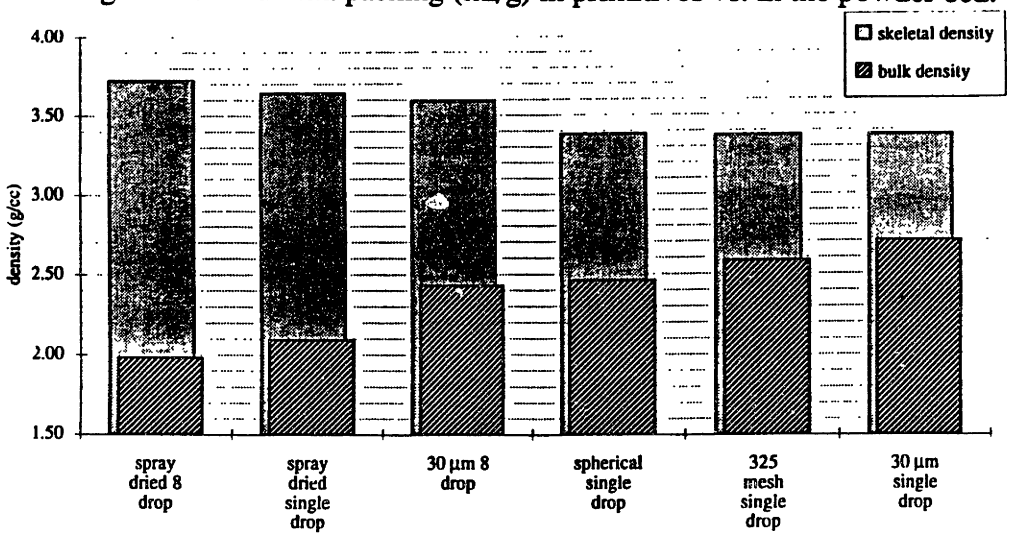

Figure 5.4 Summary of measured densities for primitives.

Predicted Primitive Size

The composition and density data for single drop primitive samples can be used to predict the diameter a individual primitive should assume. The absolute volume of silica in any primitive is fixed by the binder droplet size and can therefore be calculated easily. Dividing the absolute volume of silica present by the volume fraction of silica in a

primitive will give the total volume of the primitive. The predicted diameter of the primitive can then be compared with observed diameters from SEM analysis. Table 5.7 displays the results of these calculations.

Table 5.7 Predicted and Observed Primitive Diameters

Primitive Type	Predicted Dia. (μm)	Observed Dia. (μm)
30 μm Single Drop Primitives	32	110
325 Mesh Single Drop Primitives	33	115
Spherical Powder Single Drop Primitives	38	135
Spray Dried Single Drop Primitives	58	175

The observed diameters are larger than the predictions by a factor of approximately 3 - 3.5. This ratio remains nearly constant among all types of primitive, regardless of the predicted diameter. It is likely that a systematic experimental error is responsible for the difference between observed and predicted values, and that the results presented here are qualitatively correct. Three possible sources of experimental error exist to explain the discrepancy between the predicted and observed values. These are outlined below:

• The SEM observations are misleading: The distribution of binder in a primitive is not required to be homogeneous. It is therefore likely that particles on the outer surface of the primitives are attached only by a small silica bridge at their base. A coating of several such particles could cause the primitive diameter to appear larger than density measurements would suggest by up to two particle diameters; a significant fraction of the predicted diameter. Additionally, such particles would have little effect on the bulk density measurements if large pores were present between them.

• Closed Porosity: Closed porosity inside a primitive would not be measurable by helium pychnometry. Thus, the measured sample volume would include the volume of any closed pores leading to a measured skeletal density lower than the true value. Lower skeletal densities indicate a higher volume fraction of silica, so the reported silica content would appear higher than the actual amount. This would lead to smaller predicted diameters since the diameter calculation is based on the ratio of the absolute silica content to the silica volume fraction.

• A small, systematic error is likely to exist in the bulk density measurements due to the volume correction process for inter-primitive filling. This is due to the fact that the powder samples tend to densify as the mercury fills the chamber, thereby decreasing the pore size between particles. This pore size is then taken as a basis to remove inter-primitive filling volume. A larger true pore size between particles would result in inaccurate volume corrections, and tend to make the reported bulk density higher than the true value, in turn making the reported silica volume fraction larger. This error, however, can be estimated and could not account for more than 10% of the discrepancy between the observed and predicted diameters.

5.2 Line Densification

Lines printed into the powder bed assume a circular cross section, as seen in figures 4.28 and 4.29. Lines could not be removed from the powder bed, so density measurements were not possible. Evidence points to a surface tension mechanism at work in the lines also. First, the cross section corresponds to a minimization of surface energy given the constraint that they must be long and thin. Second, since lines are made from overlapping primitives, it is reasonable to assume that they also undergo densification by similar means. Finally, the gap between the line and the wall of the trench it lies in may indicate a volume change. The gap is larger than would be expected

from either ballistic interaction or densification alone, and is most likely due to a combination of the two phenomena.

5.3 Powder Additive Effects

Results from powder additive experiments on single line walls show the presence of acid in the powder bed has an effect on the resulting microstructure. The presence of both citric acid and polyacrylic acid reduce the thickness of printed single line walls (Figure 4.30). Higher concentrations of acid produce thinner walls, and the stronger polyacrylic acid has a greater effect than citric acid. These results can be explained by the dependence of colloidal silica stability on pH. As the pH of the binder decreases to approach neutrality, the silica begins to gel, greatly increasing binder viscosity. The gelling action prevents easy flow of binder between particles, locking it in place and producing a thinner wall with a higher silica content. From the results of these experiments, it is seen that addition of 2% polyacrylic acid can reduce wall width by up to 66% over plain powder. As binder volume/unit line length increases, however, a saturation point is reached and wall width begins to expand quickly (Curodeau, 1990). The addition of acid delays this saturation effect, but it is still visible at large values of binder volume/unit line length where the concentration of acid may be insufficient to induce complete gelation.

5.4 Line Pairing in Walls

One of the phenomena discovered in the multiple line wall experiments involved the fusing of adjacent printed lines into connected pairs. Two separate hypotheses were considered as a possible explanation for the origin of this pairing. First, that sequentially printed adjacent lines are close enough together to make an initial contact, perhaps due to the trench carved out by ballistic action of the binder jet. Once initial contact has been made, binder surface tension forces cause the two lines to consolidate. When the next

line is printed, the previous line has moved sufficiently far toward the initial line that no contact is made, so this third line does not join the first two. This process, illustrated in Figure 5.3, continues throughout each layer, giving rise to defects in the gaps between the line pairs.

The second hypothesis is concerned with aerodynamic effects generated by the motion of the printhead. Because the printhead is asymmetric, differing air currents may be cause depending on which direction it is traveling in across the powder bed. It is possible the in either one or both directions these aerodynamic effects cause a deflection of the stream either backward or forward, causing adjacent line to be printed extremely close to one another. Whether or not a pair of lines are fused or separated would depend on which direction the printhead was traveling. This process is shown in Figure 5.4.

The two hypotheses make different predictions about what should happen when several groups of lines are printed in the same layer, as was done in the wall experiments. The surface tension hypothesis predicts that all lines should be paired unless an odd number of lines is printed. In this case, the last line printed would remain unpaired. The aerodynamic hypothesis predicts that in an odd numbered group of line, either the first or the last can be unpaired, depending on the initial printhead direction. For an even number of lines, either all will be paired, or the first and last will both be unpaired.

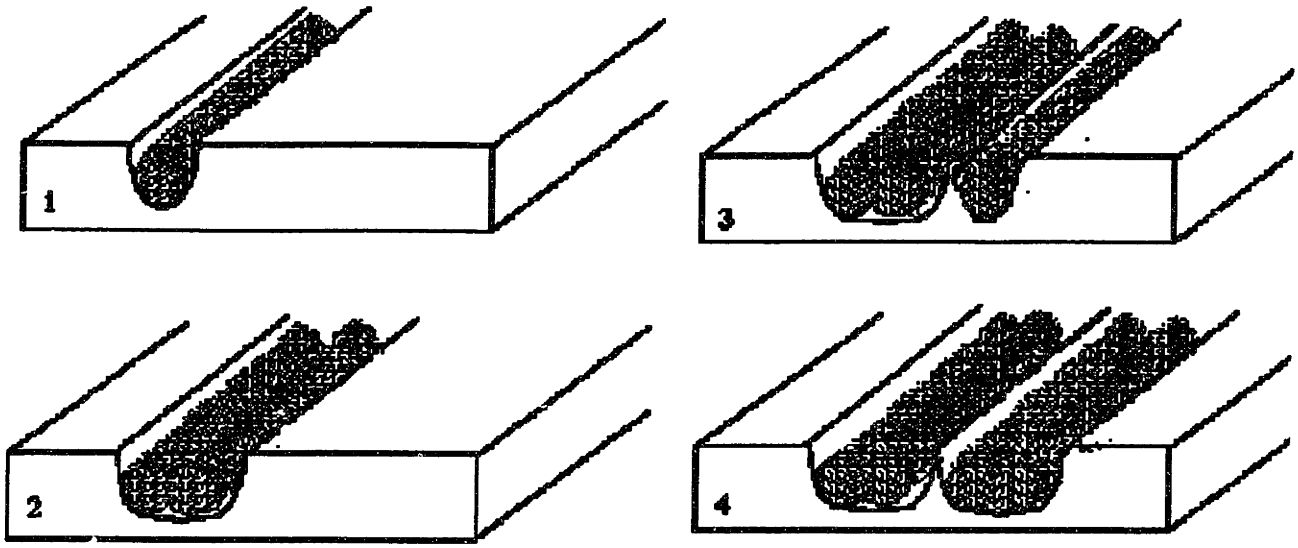

Figure 5.5. Surface tension forces cause pairs of sequentially printed lines to fuse, leaving a defect in between pairs in each layer.

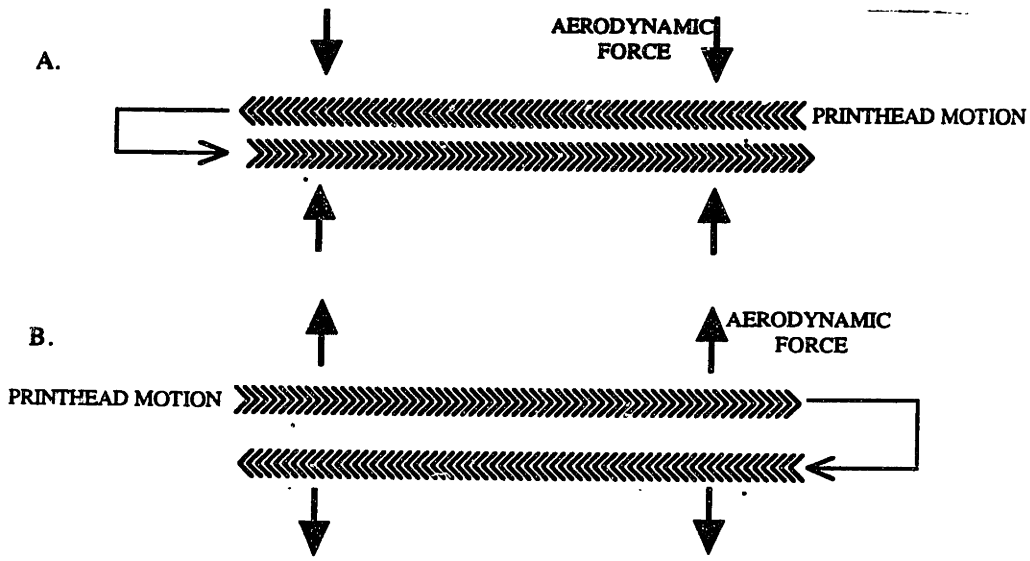

Figure 5.6. In the aerodynamic hypothesis, pairing depends on printhead direction. Assume that when the printhead moves to the left the stream is deflected toward the rear of the bed, and when it moves to the right the stream is deflected toward the front. In A above it is seen that fusing occurs when the printhead moves left to right and then back. In B, a pair of lines printed with the opposite printhead motion are further separated.

The first wall to be examined was wall 4B (refer to figure 3.9). Figure 5.5 is the micrograph of the cross section of this wall in which line pairing was first noticed. The defect is clearly visible running through the center of the wall, with a fused pair of lines on either side. The ridge at the top of the wall appears in the lower right hand corner of

the photograph. From this information, the original orientation of the wall can be deduced.

The fact that the pairs occur on either side of the central line is consistent with both hypotheses of pair formation, but it does give information about which way the aerodynamic forces must work if that hypothesis is correct. Figure 5.6 shows the predictions of the aerodynamic hypothesis, given that wall 4B has two pairs rather than one in the center with single lines on either side.

For this particular .tdp file, only two walls are predicted to look different by the different hypotheses. The aerodynamic hypothesis predicts that wall 3B and all 5B will have an unpaired line in front, while the surface tension hypothesis predicts that unpaired lines will only occur at the back of a wall. Unfortunately, no samples of wall 5B survived preparation due to fractures occurring at the notch. However, wall 3B was successfully prepared. Figure 5.7 shows a micrograph of its cross section, in which the ridge is visible in the top right corner. The line containing the ridge is also the unpaired line, occurring at the back of the wall.

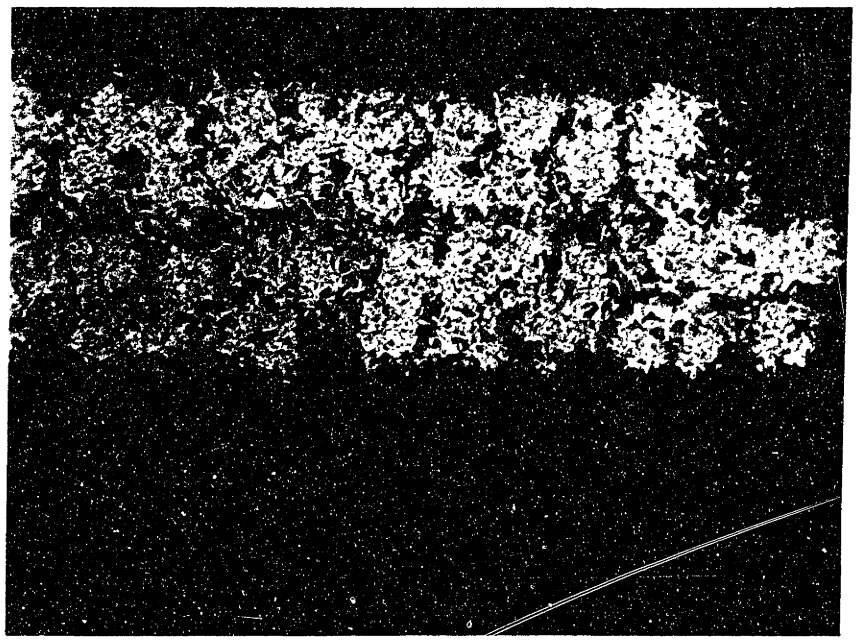

Figure 5.7 Photomicrograph of wall 4B showing pairing.

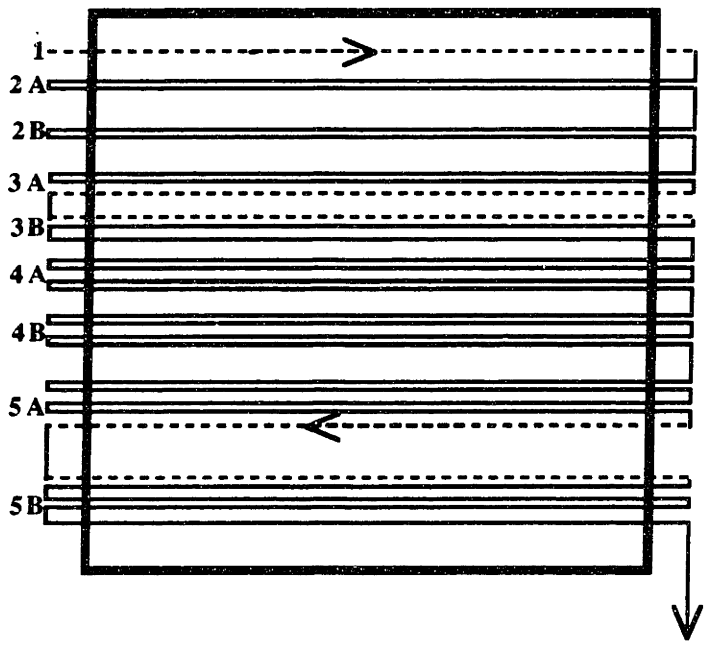

Figure 5.8 Printhead motion diagram for walls, showing predictions made by the aerodynamic hypothesis. Lines the must remain unpaired if the model is correct are shown with a dashed line.

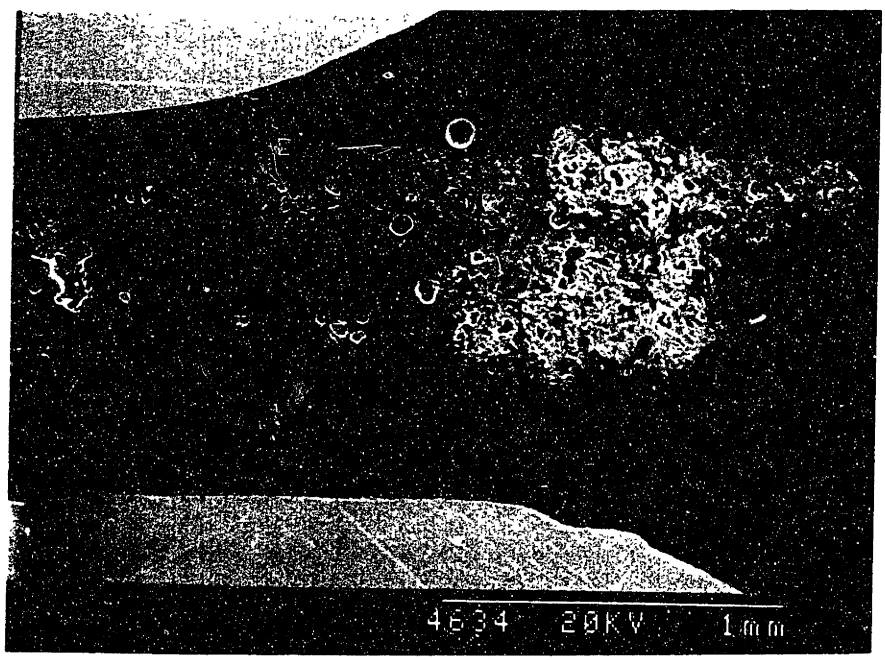

Figure 5.9 Photomicrograph of wall 3B.

The pairings observed in walls 3B and 4B are consistent only with the surface tension hypothesis. This hypothesis also explains the joining of lines observed when pairs of lines were printed into the powder bed for *in-situ* observation. There is no evidence that aerodynamic effects contribute to pairing. Additionally, the same argument can be used to rule out many other hypotheses for line pairing that share the directional feature of the aerodynamic hypotheses, such as a wobble in the fast axis slide, or a moment applied to the printhead carriage depending on the direction of travel. Thus, surface tension effects are seen to effect the microstructure bulk parts as well as that of primitives and individual lines.

6. CONCLUSIONS

Several parameters and mechanisms are found to be important in Three Dimensional Printing. The most important microstructural factor is the surface tension mechanism for densification of the loose powder. The surface tension forces of the binder exceed the cohesive strength of the powder bed, causing particle rearrangement during printing. Evidence of this is seen in the shape of primitive elements and in texturing of the bulk microstructure in full parts. Surface tension forces lead to densification of bound areas in a 3D Printed part, along with an anisotropic pore structure in the area between printed lines.

A second important parameter is powder morphology. The shape and size of the powder particles affects the extent and geometry of silica bridging between particles, the size of the primitive structure, and the local composition of the part. The bulk composition will not vary since the same volume of binder is printed into the same part area. Spherical powders produce larger, more porous primitive structures with a low silica volume fraction while faceted powders produce primitives with significant silica filling in the interparticle pores.

Finally, additives to the powder may affect the final microstructure of a printed part. Acid additives have been shown to prevent binder bleeding and to reduce the dimensions of individual printed lines. Any additive that will induce gelation in the colloidal silica binder will have a similar effect. Other parameters affecting part microstructure that were not studied include ballistic interactions, particle size distribution, and powder spreading and leveling strategies.

Understanding the factors which control microstructural development in Three Dimensional Printing makes possible the design of final part microstructure. The serial nature of 3D Printing, in which a part is built in small sections sequentially, allows great flexibility in controlling the local properties of the part. For example, by controlling

factors such as the cohesive strength of the powder bed or the extent of binder gelation it is possible to build parts with a controlled pore structure. The future use of finer charge-to-mass control of binder droplets, or proportional deflection, will allow exact placement of droplets outside the direct raster lines and greatly enhance the flexibility of microstructural control. A further possibility is the design of engineered or 'smart' powders that will respond to the printing process in ways specifically determined to affect part properties. Many specialized applications can be envisioned to utilize these capabilities, such as hot gas cross flow filters with designed in pore structures, oriented porosity in casting shells and electronic substrates for thermal control, and preforms for infiltration of other materials to produce composites with specified properties.

The use of a CAD model to specify part geometry in Three Dimensional Printing may be extendible to include microstructural properties. In such Computer Derived Microstructures, settings for the factors and mechanisms which control microstructure would be stored in a computer file with the part dimensions and implemented in real time during printing. Many other rapid prototyping technologies use processes that affect microstructure, as was shown in Chapter 2. Ideas involving control and specification of microstructure are generally applicable to the entire field of solid freeform fabrication with numerous possibilities. As the implementation of rapid prototyping technology progresses, a new engineering discipline marrying materials science, mechanical design, and information technology will be necessary to realize the full potential systems such as Three Dimensional Printing.

APPENDIX A

A.1 Spray Drying

Spray drying is an established process for producing spherical agglomerates from fine powders (Masters, 1985). It is a versatile process, fully scaleable from bench top to industrial sizes. The spray dried powder described in this thesis was produced on a laboratory-scale Spray Drier made by Niro Atomizer (Copenhagen, Denmark). Figure A.1 is a schematic diagram of this machine.

A slurry containing fine powder and possibly some sort of binder is dispersed in a liquid vehicle. The slurry is pumped into the spray drying chamber, where it is broken up into small droplets. The chamber temperature is maintained at well above 100°C, causing the liquid to evaporate. The solids contained in each droplet are agglomerated as the liquid dries, assuming a spherical shape. Airflow through the machine removes the spray dried powder and deposits it for collection.

A.2 Formulations

The starting material for spray drying was Reynolds RC172 Alumina powder. The average particle size for this powder is 0.8 μm, with few particles larger than 1 μm, but in the dry state it is extensively agglomerated. 2000 g of powder were used for a typical run. The powder was added to enough deionized (DI) water to produce a solid volume fraction of 25%. The DI water was treated in advance with a solution of polyacrylic acid (MW 90,000). The polyacrylic acid was present in concentrations equal to 2% by weight of the mass of the alumina powder. The acid served both as a dispersant for the alumina slurry, and as a binder in the spray drying process. Polyacrylic acid was chosen due to its effectiveness as an anti-bleeding additive for 3D Printing.

The powder was added to the acidified water in the as-received state, so the initial slurry was extensively flocculated due to the large agglomerates of alumina. To correct this problem, the slurry was placed on a ball mill for 24 hours. The milling media

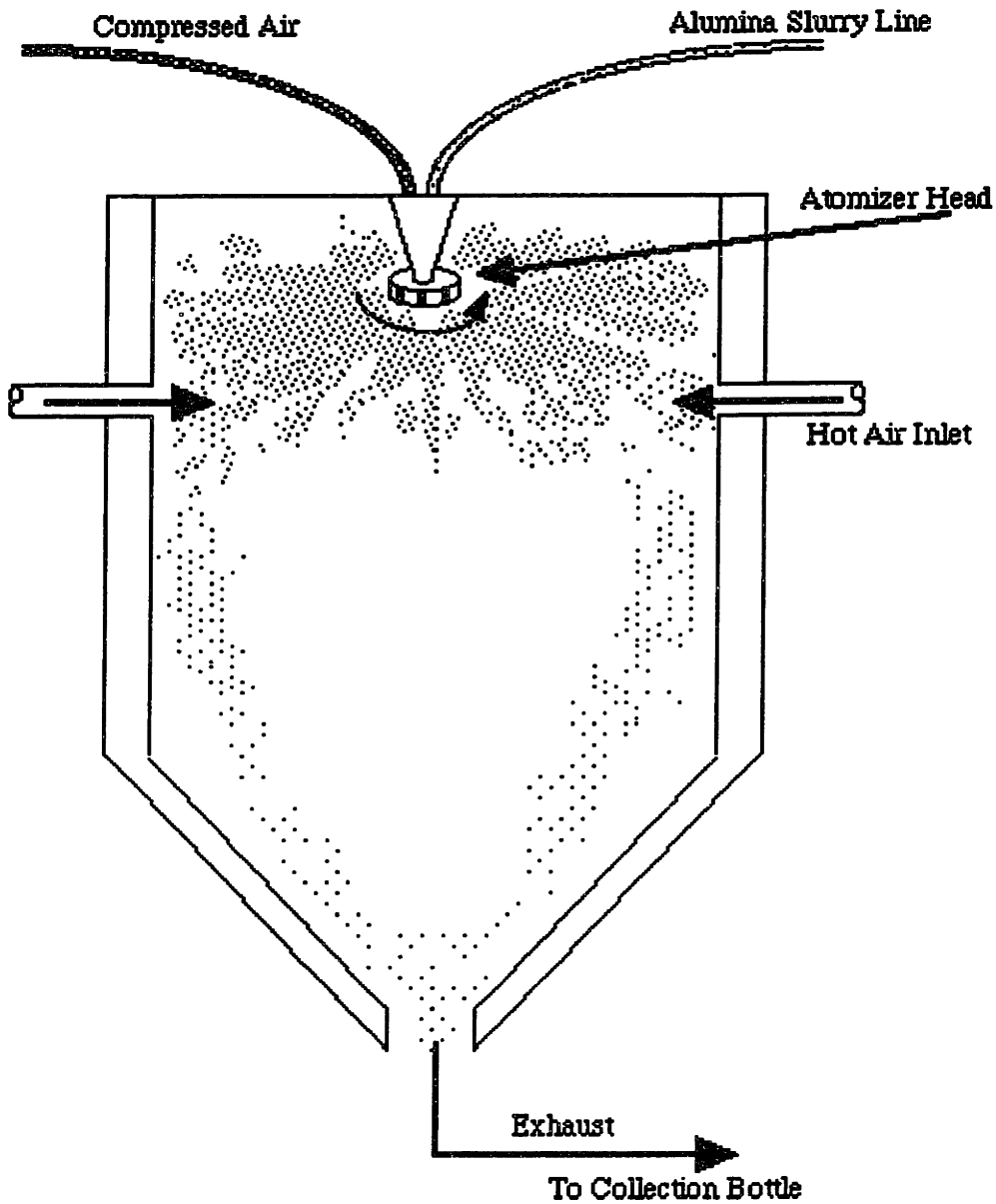

Figure A.1 Spray Drying Apparatus.

consisted of alumina balls between 1 and 3 cm in diameter. After milling, the slurry was treated with an ultrasonic horn to break any remaining agglomerates. The slurry was then allowed to settle for one hour to remove any remaining particles large enough to fall out of suspension during spray drying. The remaining slurry was estimated to have a solid volume fraction of 22%. Finally, 2 drops of octanol were added as a defoaming agent.

The slurry was pumped into the spray drier using a peristaltic pump set at a flow rate of approximately 45 ml/min. The turbine on the aspirator head was driven by compressed air from the house line at pressures that varied between 80 and 100 psi. Hot air inlet temperature was maintained at 300°C, and exhaust temperature at 110°C. Spray dried powder was removed from the collection bottle and stored in an oven at 80°C until all the powder had been collected. It was then weighed and bottled for use. Typical yields were around 80%.

The product obtained was a spherical alumina powder, from 8 to 20 μm in diameter. The variation in size is attributed to the cycling of the house compressor causing the turbine speed to vary during the process. Some defects, such as hollow or dimpled particles were observed. The powder showed excellent flowability, and was found to have a density of 3.82 g/cc.

REFERENCES

Alvin, Mary Anne, Thomas E. Lippert, Jay E. Lane,"Assessment of Porous Ceramic Materials for Hot Gas Filtration Applications," *Cer Bul* , Sep. 1991.

Ashley, Steven, "Rapid Prototyping Systems," 1990.

Bourell, D.L., J.J. Beaman, H.L. Marcus, J.W. Barlow, "Solid Freeform Fabrication An Adanced Manufacturing Approach"; pp. 1-7 in Proceedings, Solid Freeform Fabrication Symposium, Austin, TX, 1990.

Cima, M.J., and E. Sachs,"Three Dimensional Printing: Form, Materials, and Performance"; in Proceedings of the Solid Freeform Fabrication Symposium, Austin, TX, 1991.

Curodeau, Alain as cited in Esterman (1990), pp. 33-37.

Eagar, T.W., "An Overview of the Design - Prototype - Manufacturing Protocol," presented at the Materials Processing Center Spring Symposium on Prototyping: Rapid Paths to Market, Massachusetts Institute of Technology, Cambridge, MA, 1992.

Esterman, Marcos, "Characterizationof the Powder/Binder Interaction in three Dimensional Printing"; SM Thesis. Dept. Mech. Eng., Massachusetts Institute of Technology, August 1990.

Fan, T.,A. Lauder, E. Sachs, and M.J. Cima, "The Surface Finish in Three Dimensional Printing," presented at the Third International Conference on Rapid Prototyping, University of Dayton, Dayton, OH 1992.

Flach, Lawrence and Richard P. Chartoff, "A Computer Model For Laser Photopolymerization"; pp. 155-163 in Proceedings, Solid Freeform Fabrication Symposium, Austin, TX, 1990.

Hise, O'Neal, McNeal, and Parasuraman, "The Effect of Product Design Activities on Commercial Success Levels of New Industrial Products," *J. of Product Innovation Management*, Vol. 6 (1992).

Hom, Stephen, "Prototyping: Paths to the Present"; ME Thesis. Dept. Mech. Eng., Massachusetts Institute of Technology, p. 118, Feb. 1991

Iler, R.K., The Chemistry of Silica. J. Wiley and Sons, New York, 1979.

Lakshminarayan, Uday, Stan Ogrydiziak, and H.L. Marcus, "Selective Laser Sintering of Ceramic Materials"; pp. 16-26 in Proceedings, Solid Freeform Fabrication Symposium, Austin, TX, 1990.

Lauder, A., M.J. Cima, E. Sachs, and T. Fan,"Three Dimensional Printing: Surface Finish and Microstructure of Rapid Prototyped Components"; in Proceedings, Synthesis and Processing of Ceramics: Scientific Issues, Boston, MA, 1991.

Lee, S. John, "Powder Layer Generation for Three Dimensional Printing"; SM Thesis. Dept. Mech. Eng., Massachusetts Institute of Technology, May 1992.

Manriquez-Frayre, J.A., and D.L. Bourell, "Selective Laser Sintering of Binary Metallic Powder"; pp. 99-106 in Proceedings, Solid Freeform Fabrication Symposium, Austin, TX, 1990.

Marcus, Harris L., Joseph J. Beaman, Joel W. Barlow, and David L. Bourell,"From Computer to Component in 15 Minutes: The Integrated Manufacture of Three Dimensional Objects," *JOM* , April 1990.

Masters, K., Spray Drying Handbook, 4th ed. J. Wiley and Sons, New York, 1985.

Michaels, S., E. Sachs, M. Cima, "Metal Parts Generation by Three Dimensional Printing", to be presented at the Solid Freeform Fabrication Symposium, Austin, TX, 1992.

Qualls, William, Richard W. Olshavsky and Ronald E. Michaels, "Shortening of the PLC: An Empirical Test," *J. of Marketing*, Fall 1981.

Rapid Protoyping Monitor , "Technology Focus: Laminated Object Manufacturing," Vol. 1 (1), pp. 1-6, June 1991.

Sachs, E., M. Cima, P. Williams, and D. Brancazio, "Rapid Tooling and Prototyping by Three Dimensional Printing"; pp. 41-45 in Transactions NAMRI/SME, 1990.

Sachs, Emanuel, Michael Cima, James Bredt, Alain Curodeau,"CAD-Casting: The Direct Fabrication of Ceramic Shells and Cores by Three Dimensional Printing," accepted for publication in *Manufacturing Review*, to appear June, 1992.

Shaw, Duncan, Introduction to Colloid and Surface Chemistry. Butterworths, Boston, MA, 1966.

Staelin, David, "A Strategic Approach to Rapid Prototyping for Products and Processes," presented at the Materials Processing Center Spring Symposium on Prototyping: Rapid Paths to Market, Massachusetts Institute of Technology, Cambridge, MA, 1992.

Zong, G.-S., R. Carnes, H.G. Wheat, and H.L. Marcus, "Solid Freeform Fabrication by Selective Area Laser Deposition"; pp. 83-90 in Proceedings, Solid Freeform Fabrication Symposium, Austin, TX, 1990.